TECTONICS, VOL. 26, TC2003, doi:10.1029/2006TC001960, 2007

Click Here for Full Article

Oblique indentation in the Eastern Alps: Insights from laboratory experiments

C. L. Rosenberg,[1] J.-P. Brun,[2] F. Cagnard,[2] and D. Gapais[2]

Received 28 February 2006; revised 14 November 2006; accepted 17 November 2006; published 10 March 2007.

[1] Experimental models scaled for density and viscosity were performed to investigate the effects of indentation obliquity and rheological stratification on the deformation patterns caused by continental indentation. The shape and orientation of the indenter were inspired by the Dolomites indenter of the southern Europeans Alps. The results of our experimental models showed that small changes in the angle of convergence induce marked differences in the patterns of deformation. The only models whose fault patterns satisfyingly reproduced that of the Eastern Alps were characterized by NNE directed motion of the indenter. In these models, E-W extension formed in front of the leading edge of the indenter, as observed in the Eastern Alps along the Brenner extensional fault. Extensional deformation of the models maintained compatibility between the areas located on both sides of the indenter edge, which shortened at different rates and in different directions. Therefore extension was not caused by gravitational instabilities but by the kinematic and geometrical boundary conditions imposed by the indenter shape and the convergence direction. Lateral escape was always modest in our models, reaching a maximum of 20%. This value is much smaller than previous estimates of lateral escape in the Eastern Alps but very close to the amount inferred by our reassessment of Tertiary E-W extension in the Eastern Alps. **Citation:** Rosenberg, C. L., J.-P. Brun, F. Cagnard, and D. Gapais (2007), Oblique indentation in the Eastern Alps: Insights from laboratory experiments, *Tectonics*, *26*, TC2003, doi:10.1029/2006TC001960.

1. Introduction

[2] Indentation of continental plates and microplates involves the penetration of a relatively stiff plate into a weaker and larger continent during collision. The length of continental indenters varies from hundreds of kilometers, as in the Alps [*Ratschbacher et al.*, 1991b], to thousands of kilometers, as in the Indian-Asian collisional system [*Molnar and Tapponnier*, 1977]. Deformation propagates into the indented lithosphere far away from the plane of collision, over distances of the same order of magnitude as the indenter length [*England and Houseman*, 1989; *Houseman and England*, 1993], as suggested for the Indian indentation, which extends from the Himalayan front to the Baikal Rift [*Cobbold and Davy*, 1988].

[3] Indentation is inferred to have affected the deformation fields of some ancient [e.g., *Jacobs and Thomas*, 2004] and present-day plate margins [e.g., *Lu and Malavieille*, 1994], leading to lithospheric thickening in the indented continent [*Davy and Cobbold*, 1988], to large-scale rotations around vertical axes [*England and Molnar*, 1990], and to lateral motions, subparallel to the indenter front, within the indented continent. The following mechanisms have been suggested to explain these displacements [see *Robl and Stüwe*, 2005a]: (1) convergence between plates that induces lateral motions directed away from the area of convergence [*Tapponnier et al.*, 1982]; (2) gravity-driven flow reducing lateral contrasts in gravitational potential energy [*Rey et al.*, 2001]; and (3) a combination of the previous two processes. The first mechanism was termed lateral escape [*Tapponnier et al.*, 1982], the second one was termed extensional, or gravitational, collapse [*Dewey*, 1988; *Rey et al.*, 2001], and the third was termed lateral extrusion [*Ratschbacher et al.*, 1991a]. Following *Houseman and England* [1993], we will use the more descriptive term lateral displacement or lateral motion, when referring to all three types of deformation.

[4] Lateral displacements in front of an orogenic indenter are usually asymmetrically distributed, with most, if not all of the orogen-parallel displacements directed toward one end of the indenter margin, as inferred for the Eastern Alps and for the Tibetan region. However, in some cases, as in front of the Arabian plate, two opposite directions of lateral motion are observed. The amount and the direction of escape are generally assumed to be controlled by the strength of the lithosphere in the area accommodating escape [*Davy and Cobbold*, 1988], but several other factors also affect the process of lateral escape: (1) the size of the indented continent [*Davy and Cobbold*, 1988]; (2) the type of tectonic setting affecting the areas accommodating lateral displacement, e.g., extension perpendicular to the direction of lateral motion enhances lateral displacements [*Martinod et al.*, 2000]; (3) the strength of the lithosphere in front of the indenter [*Davy et al.*, 1995]; (4) indentation obliquity [*Ratschbacher et al.*, 1991a; *Houseman and England*, 1993; *Robl and Stüwe*, 2005a], i.e., the angle between the plane of collision and the convergence direction; and (5) convergence obliquity, i.e., the angle between the convergence

[1] Institut für Geologische Wissenschaften, Freie Universität Berlin, Berlin, Germany.
[2] Géosciences Rennes, UMR 6118 CNRS, Université Rennes I, Rennes, France.

0278-7407/07/2006TC001960$12.00

direction and the northern and lateral boundaries of the deforming model.

[5] The extent to which the direction and magnitude of lateral displacements are controlled by the obliquity of the indenter motion is not known. It is the aim of this paper to experimentally study the effects of this parameter on the fault pattern and on the amount of lateral motion of the indented plate. The boundary conditions chosen for the present experiments are inspired from the Tertiary Eastern Alps. Therefore we will compare the experimental results with the fault patterns of the Eastern Alps and discuss which boundary conditions are more appropriate to explain the spatial distribution of thickening and orogen-parallel extension in the Eastern Alps. The factors determining the specific sites and causes of extension will also be examined.

2. Tertiary Tectonics of the Eastern Alps

[6] The Tertiary structural pattern of the Eastern Alps is well constrained by field-based structural investigations [e.g., *Behrmann*, 1988; *Selverstone*, 1988; *Ratschbacher et al.*, 1991b; *Polinski and Eisbacher*, 1992; *Decker et al.*, 1994; *Linzer et al.*, 1997; *Peresson and Decker*, 1997; *Frisch et al.*, 1998; *Linzer et al.*, 2002]. These studies documented contemporaneous N-S shortening and east directed extension of a crustal wedge confined by the sinistral Salzach-Ennstal-Mariazell-Puchberg (SEMP) Fault in the north and the dextral Pustertal Fault in the south (Figures 1a and 1b). In spite of unanimous agreement on this interpretation, the absolute amounts of displacement along the faults bounding the South Alpine indenter, and the total amount of lateral motion are still a subject of debate. These data are of prime importance for defining the boundary conditions of our models and for extrapolating our model results to nature. Below, we discuss and reassess the amount of Tertiary displacements along such faults.

2.1. Tertiary E-W Extension in the Eastern Alps: How Much?

[7] Tertiary E-W extension in the Eastern Alps [e.g., *Royden*, 1988; *Ratschbacher et al.*, 1991a] was inferred to have attained 40 to 50% [*Ratschbacher et al.*, 1991b; *Frisch et al.*, 1998]. These values are consistent with the inferred small volumes of eroded rocks in the Tertiary Perialpine basins, suggesting that E-W extension was the prime mechanism driving Tertiary exhumation [*Kuhlemann et al.*, 2001]. In contrast, *Huismans et al.* [2001] estimated a lateral displacement in the range of only 0 to 50 km, which corresponds to 0 to 16% of extension. These values were estimated by subtracting the inferred amount of Miocene extension in the Pannonian Basin from the restored amount of Miocene convergence in the Carpathians. The resulting value constrains the space available within the Pannonian Basin to accommodate the eastward motion of the Eastern Alps [*Huismans et al.*, 2001]. On the basis of independent lines of evidence, we also find that the amount of Tertiary extension in the North Calcareous Alps, and in the rest of the Eastern Alps did not exceed 20%. This conclusion relies on the following observations:

[8] 1. The carefully considered retrodeformation of the North Calcareous Alps to their Oligocene state [*Linzer et al.*, 2002] (Figure 2) indicates 22% of Tertiary E-W extension. This is illustrated by the increase in length of the dashed line between points A and B in Figure 2. However, transpressive deformation of the North Calcareous Alps resulted in a lateral offset of markers along faults in map view larger than the effective lateral displacement of these faults. For this reason, *Ortner* [2003] suggested that sinistral displacement along the Inntal Fault was 40 km instead of 65 km. Thus the value of 22% inferred above may be an overestimate.

[9] 2. E-W extension in the central part of the Eastern Alps (Figure 2a) is almost entirely accommodated in the Tauern Window [*Linzer et al.*, 2002, Figure 10]. The amount of extensional displacement along the Brenner normal fault (Figures 1a and 1b) was initially estimated to 10–20 km [*Behrmann*, 1988; *Selverstone*, 1988] but later extended to at least 25–35 km [*Selverstone et al.*, 1995], then to 50 km [*Axen et al.*, 1995], and finally to as much as 70 km [*Fügenschuh et al.*, 1997]. These values were obtained by calculating the vertical offset between hanging wall and footwall of the Brenner Fault, on the basis of thermal and/or barometric data, and by calculating the fault-parallel extensional displacement required to match this offset. The orientation of the fault plane was taken to be the present-day orientation of the Brenner Fault. Using the same principle, *Genser and Neubauer* [1989] estimated that extension along the eastern end of the Tauern Window was about 18 km. Taken together, these values yield a total of 78 km horizontal (not along the fault planes) extension, hence 26% of the central transect of the Eastern Alps (Figure 2a). However, the estimates above completely ignore that part of the observed metamorphic discontinuity across the Brenner Fault is the result of upright folding within the Tauern Window (Figures 1b and 1c), i.e., pronounced folding and erosion east of the Brenner Fault, but no folding west of this fault, where no indentation occurred (Figure 1a). Hence the amount of extension is systematically overestimated in the studies above. In spite of the widespread occurrence of extensional fabrics in the western Tauern Window, erosion of its high-amplitude antiforms (Figure 1c) [*Schmid et al.*, 2004] is sufficient to exhume the Tauern Window almost to its presently exposed structural level.

[10] 3. The inferred amount of E-W extension along the southern part of the Eastern Alps (Figure 2a) results mainly from displacement along the Lavanttal fault, the Hochstuhl Fault, the Mölltal Fault, and the Iseltal Fault (Figures 1, 2a, and 2b) [*Linzer et al.*, 2002]. Previous estimates of E-W extension based on the offsets of markers along these faults in map view suggested 40 km displacement for the Mölltal fault, 20 km for the Iseltal Fault, and 20 km for the Hochstuhl Fault [*Linzer et al.*, 2002]. However, these displacements are overestimated. The boundary of the Tauern Window shows an apparent lateral offset of only 23 km along the transpressive Mölltal Fault (Figure 1b) [*Exner*, 1962; *Kurz and Neubauer*, 1996]. The marker used

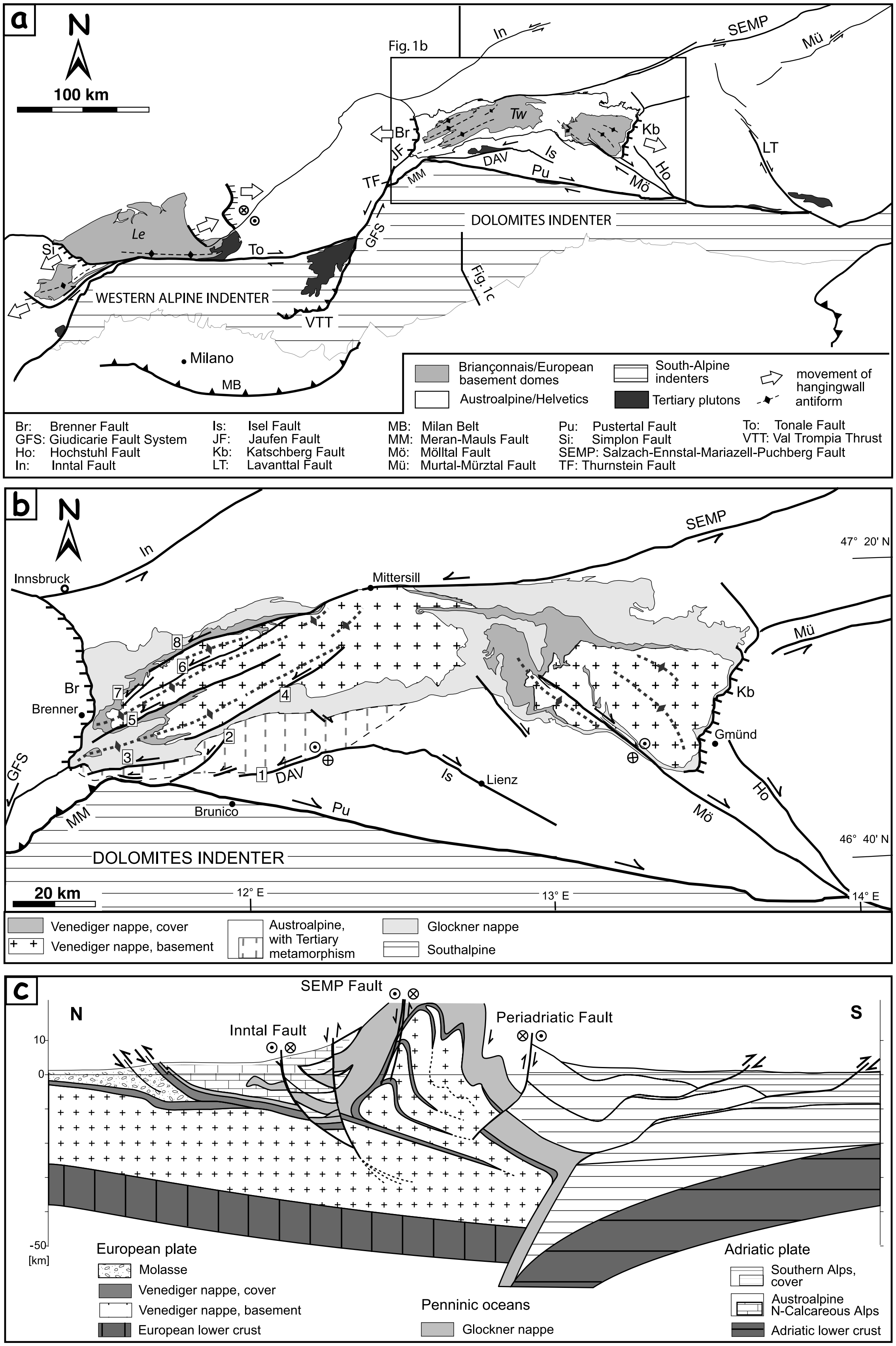
a
N
100 km
Fig. 1b
In
SEMP
Mü
Tw
Br
JF
Kb
Is
DAV
LT
TF
MM
Pu
Mö
Ho
DOLOMITES INDENTER
Le
Si
To
GFS
Fig. 1c
WESTERN ALPINE INDENTER
VTT
Milano
MB
Briançonnais/European basement domes
Austroalpine/Helvetics
South-Alpine indenters
Tertiary plutons
movement of hangingwall
antiform
Br: Brenner Fault
GFS: Giudicarie Fault System
Ho: Hochstuhl Fault
In: Inntal Fault
Is: Isel Fault
JF: Jaufen Fault
Kb: Katschberg Fault
LT: Lavanttal Fault
MB: Milan Belt
MM: Meran-Mauls Fault
Mö: Mölltal Fault
Mü: Murtal-Mürztal Fault
Pu: Pustertal Fault
Si: Simplon Fault
SEMP: Salzach-Ennstal-Mariazell-Puchberg Fault
TF: Thurnstein Fault
To: Tonale Fault
VTT: Val Trompia Thrust
b
N
In
SEMP
47° 20' N
Innsbruck
Mittersill
Mü
Br
Brenner
Kb
Gmünd
GFS
DAV
Is
Lienz
Brunico
Pu
Mö
Ho
MM
46° 40' N
DOLOMITES INDENTER
20 km
12° E
13° E
14° E
Venediger nappe, cover
Venediger nappe, basement
Austroalpine, with Tertiary metamorphism
Glockner nappe
Southalpine
c
SEMP Fault
N
Inntal Fault
Periadriatic Fault
S
10
0
-50
[km]
European plate
Molasse
Venediger nappe, cover
Venediger nappe, basement
European lower crust
Penninic oceans
Glockner nappe
Adriatic plate
Southern Alps, cover
Austroalpine N-Calcareous Alps
Adriatic lower crust

Figure 1

to estimate the offset along the Iseltal fault is merely an erosional contact between basement and cover. Its apparent offset in map view is ∼10 km, but the effective displacement may be much smaller. The lateral offset along the NNE striking Hochstuhl fault (Figure 1b) is less than 5 km [*Polinski and Eisbacher*, 1992]; hence its E-W component of extension is negligible. Additional, but small and yet undefined, components of E-W extension may be accommodated along the dextral Lavanttal Fault (Figure 1a) and sinistral Defereggen-Antholz-Vals (DAV) Fault (Figure 1b). The only significant component of extension along this southern portion of the Eastern Alps (Figure 2a) results from dextral displacement along the Pustertal Fault (Figures 1a and 1b) of about 30–40 km [*Polinski and Eisbacher*, 1992]. In summary, E-W extension greater than 20% within the southern segment of the Eastern Alps (Figure 2) is unlikely.

2.2. Inferred Kinematics and Absolute Amounts of Displacement Along the Giudicarie Fault System

[11] The Giudicarie Fault System (GFS, Figures 1a and 1b) marks the western boundary of the South Alpine Dolomites indenter [*Frisch et al.*, 2000]. It is a sinistral transpressive structure [*Werling*, 1992], which transfers shortening in the Val Trompia fold and thrust belt (VTT in Figure 1a) to the NE striking thrusts of the Meran-Mauls fault (Figure 1b), and according to some authors [*Cornelius*, 1940; *Laubscher*, 1988; *Schmid et al.*, 2004] to the E-NE striking, upright folds of the Tauern window (Figures 1a, 1b, and 1c).

[12] The total amount of sinistral displacement accommodated by the GFS in Oligo-Miocene time is still debated [e.g., *Prosser*, 1998; *Viola et al.*, 2001; *Schmid et al.*, 2004]. One interpretation [*Schönborn*, 1992; *Frisch et al.*, 1998, 2000; *Linzer et al.*, 2002] suggests that the present-day length (70 km) of the GFS, between Tonale Fault and Pustertal Fault (Figures 1a and 1b) represents the amount of Tertiary lateral displacement along this fault. This interpretation is supported by balanced cross sections, showing that the Val Trompia thrust system, into which the GFS bends and terminates (VTT in Figure 1a), accommodated 87 km of post-Eocene-Oligocene N-S shortening [*Schönborn*, 1992]. Hence retrodeformation of the southern Alps to its early Oligocene configuration would result in a collinear geometry of the Tonale Fault and the Pustertal Fault [*Schönborn*, 1992] (Figure 1a).

[13] Alternative interpretations suggest that sinistral displacements along the GFS in the Tertiary were not more than 30–40 km [*Picotti et al.*, 1995; *Castellarin et al.*, 2006] or even as small as 15 km [*Viola et al.*, 2001]. This conclusion is based on the following arguments: (1) shortening accommodated by the Val Trompia thrusts [*Picotti et al.*, 1995] is inferred to be less than in the model of *Schönborn* [1992]; (2) mylonites of the Jaufen and Thurnstein faults (Figure 1a), which are offset by the GFS, point to a relative displacement of no more than 20 km [*Viola et al.*, 2001], provided that both shear zones were part of one continuous shear zone before the onset of sinistral motion along the Giudicarie fault; and (3) tonalitic bodies contain a 20 km long gap along the North Giudicarie fault, whereas they are almost continuously exposed along the remaining parts of the GFS [*Viola et al.*, 2001]. However, these arguments are partly ambiguous, because (1) the different estimates of shortening in the Val Trompia thrusts rely on different interpretations of field data [cf. *Schönborn*, 1992; *Picotti et al.*, 1995] and (2) the inferred spatial and kinematic continuity between the Jaufen and Thurnstein faults (Figure 1a) prior to sinistral movement along the Giudicarie Fault is questionable because the kinematics of these faults are different. Stretching lineations plunge gently to steeply from southwest to northwest in the Jaufen mylonites, whereas they are only subhorizontal and ENE striking in the Thurnstein mylonites [*Viola et al.*, 2001, Figure 4]. Finally, late Miocene shortening of approximately 80 km along the Milan Belt (MB in Figure 1a) does not continue east of the GFS [*Laubscher*, 1988], suggesting that a differential northward displacement on the order of 80 km must be accommodated along the GFS in Miocene time [*Laubscher*, 1988].

2.3. Inferred Direction of Indenter Convergence

[14] The inferred convergence direction of the Dolomites indenter varies from study to study. To explain the diversity of structures and fault kinematics north of the indenter, some authors suggested a two-phase convergence history [*Polinski and Eisbacher*, 1992; *Neubauer et al.*, 1999]. Sinistral ENE and NE striking faults were inferred to form in response to an early phase of NW directed shortening, followed by ENE to NE striking dextral faults, formed in a second stage as a result of NNE directed convergence. Sandbox experiments [*Viola et al.*, 2004] showed that the Miocene fault pattern of the GFS was best reproduced by NNE directed convergence of the Dolomites indenter,

Figure 1. Tectonics and geology of the Eastern Alps. (a) Simplified tectonic map of the Alps, after *Handy et al.* [2005] and *Viola et al.* [2001], showing the major Tertiary fault systems. Le, Lepontine dome; Tw, Tauern Window. Stippled line indicates the trace of cross section of Figure 1c. (b) Simplified tectonic map of the Eastern Alps, with boundaries after *Bigi et al.* [1990]. Fault abbreviations are as in Figure 1a and DAV, Defereggen-Antholz-Vals. Numbers indicate the references used to compile sinistral faults in the western Tauern Window: 1, *Borsi et al.* [1978] and *Kleinschrodt* [1987]; 2, *Mancktelow et al.* [2001]; 3, *Kurz et al.* [2001] and *Mancktelow et al.* [2001]; 4, modified after *Linzer et al.* [2002]; 5, *Behrmann* [1988], *Barnes et al.* [2004]; 6, *Lammerer and Weger* [1998]; 7, *Lammerer and Weger* [1998]; and 8, modified after *Linzer et al.* [2002]. (c) N-S cross section of the Eastern Alps from *Schmid et al.* [2004], across the western Tauern Window (dashed line in Figure 1a), based on surface and seismic data (TRANSALP Line).

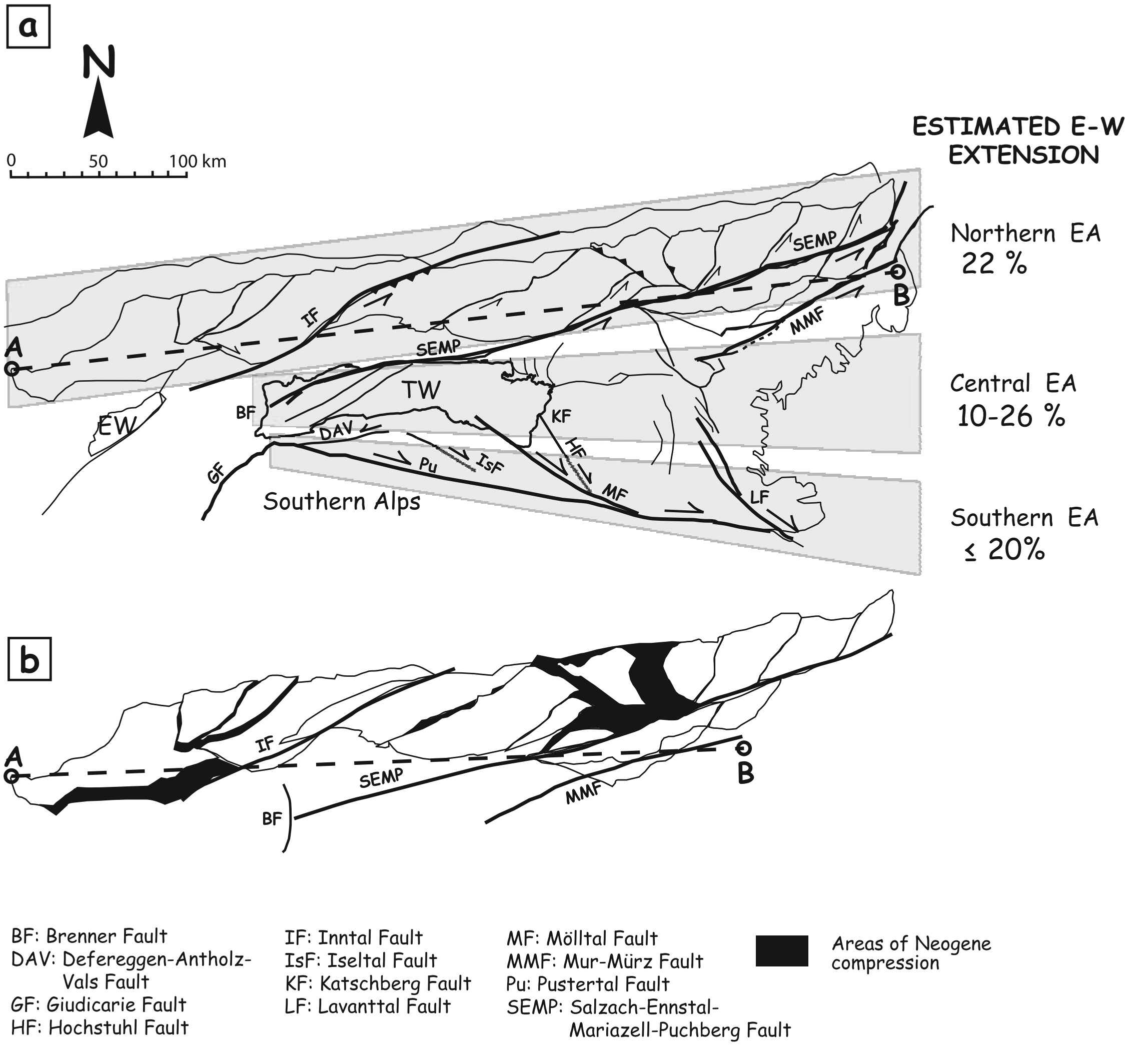

Figure 2. Retrodeformation of the Eastern Alps (EA) to their Oligocene state [see *Linzer et al.*, 2002]. (a) Simplified tectonic map of the Eastern Alps. Dashed line between points A and B is a reference line, used to estimate E-W horizontal extension by comparing its length with that of the pre-Miocene configuration in Figure 2b. E-W Extension is estimated separately for the three areas with gray shading, which we refer to as the northern Eastern Alps, central Eastern Alps, and southern Eastern Alps. (b) Simplified tectonic map of the North Calcareous Alps restored to its Oligocene configuration. The length change of the stippled line between points A and B compared to Figure 2a indicates 22% of E-W extension in the North Calcareous Alps (see text for details).

applied on a model containing a preexisting NE striking fault.

[15] Other interpretations considered that all structures formed in response to a single convergence event, but there is no agreement on the orientation of this direction. Most authors suggested a NW directed convergence [*Lammerer*, 1988; *Ratschbacher et al.*, 1989; *Sperner et al.*, 2002; *Handy et al.*, 2005] consistent with large-scale paleomagnetic reconstructions which point to sinistral rotation of the southern Alps in the Oligo-Miocene [e.g., *Vanossi et al.*, 1994]. However, a NNW directed motion [*Neubauer*, 1988; *Mancktelow and Pavlis*, 1994; *Frisch et al.*, 2000], a north directed motion [*Ratschbacher et al.*, 1991a], and a NE directed motion [*Linzer et al.* 2002, Figure 10] were also inferred.

3. Previous Experimental Work

[16] Numerous experiments were used to investigate the deformation caused by rigid indenters into crustal and/or lithospheric models. A first group of experiments was performed to study the effect of indentation into a uniform,

nonlinear viscous material (plasticine), unconfined on one side, in order to model the fault patterns of the India-Asia collision [*Tapponnier et al.*, 1982; *Peltzer*, 1988]. These experiments showed that indentation induces lateral escape of plasticine wedges that are confined by conjugate strike-slip faults striking at high angles to the shortening direction. Later indentation experiments [*Davy and Cobbold*, 1988; *Davy et al.*, 1990; *Sornette et al.*, 1993] were performed with a rheologically stratified lithosphere, consisting of silicone and sand layers scaled for density and viscosity. These experiments enabled the investigation of the relationship between thickening and lateral motion, which was shown to depend mainly on the strength of the lateral confinement, and to a lesser amount on the size of the indented continent [*Davy and Cobbold*, 1988]. Weaker lateral confinements and longer continents permit greater amounts of lateral displacements [*Davy and Cobbold*, 1988]. A similar experimental approach was used to study the Tertiary tectonics of the Eastern Alps [*Ratschbacher et al.*, 1991a], specifically investigating the effect of indenter geometry (triangular versus square geometries) and the strength of the eastern boundary of the model on the patterns of faulting. The authors suggested that square indenters and weak lateral confinement yield the closest similarities to the fault pattern of the Eastern Alps. The effects of indenter shape and size of the continent on the distribution of thickening were also investigated using thin viscous sheet models [*Houseman and England*, 1993]. These experiments showed that (1) thickening in front of the indenter is reduced if the distance between indenter and northern margin of the continent is increased; (2) thickening is less pronounced if the eastern margin is allowed to deform; and (3) oblique indentation, i.e., an indenter front oblique to the northern boundary of the model and to the convergence direction, induces an asymmetric distribution of thickening around the indenter. Thin viscous sheet models were also used to show that an increase in the obliquity of indentation increases the size of the extrusion corridor in the indented continent [*Robl and Stüwe*, 2005a]. The latter study also showed that the site of maximum thickening is controlled by the viscosity ratio between foreland and indenter, and by the aspect ratio of the indenter.

[17] Lateral variations of thickness [*Sokoutis et al.*, 2000] and viscosity [*Willingshofer et al.*, 2005] of the indented lithosphere have also been investigated and compared to the structural pattern of the Eastern Alps. The inclusion of an orogen-parallel weak zone increased the amount of lateral displacement and induced a transition from lithospheric thrusting to folding [*Willingshofer et al.*, 2005], whereas lateral variations of crustal thickness in directions at high angles to the long axis of the orogen were shown to induce transverse strike-slip structures, as observed in the Eastern Alps (e.g., the Lavanttal Fault, LT in Figure 1a [*Sokoutis et al.*, 2000]).

[18] We describe below the results of experiments conducted to test the effect of different convergence directions of the indenter on the deformation pattern of the Eastern Alps. Oblique indentation in previous experiments [*Ratschbacher et al.*, 1991a; *Houseman and England*, 1993; *Robl and Stüwe*, 2005a] was modeled by varying the angle between indenter front and northern boundary of the model, keeping the angle between the imposed convergence direction and the fixed boundaries of the model constant. As a consequence, different degrees of obliqueness corresponded to different geometries of the indenter [e.g., *Houseman and England*, 1993, Figures 1 and 2]. In the present study we investigate the indentation obliqueness by varying the movement direction of the rigid indenter with respect to the indenter front and to the margins of the deformable model (Figure 3a), maintaining a constant geometry of the indenter and a constant angle between the indenter front and the fixed margins of the model (Figure 3a). Hence the indenter shape and the obliqueness angle are not coupled in these experiments and their effects on the deformation patterns can be studied separately.

[19] These models will allow us to proof the aforementioned different hypotheses concerning the convergence direction of the Dolomites indenter. In addition we discuss below a series of experiments performed with different rheological stratifications. The motivation for these experiments was to model lateral strength variations, which are inferred to occur in the Eastern Alps as a consequence of changes in crustal thicknesses [e.g., *Ebbing et al.*, 2001], both along N-S and E-W sections.

4. Experimental Materials and Boundary Conditions

[20] Laboratory experiments scaled for density and viscosity were carried out in a Plexiglas box of $80 \times 50 \times 12$ cm (Figure 3a). The model lithosphere consisted of a ductile mantle layer of silicone, with density 1.45 g/cm^3 and viscosity 6.0×10^4 Pa s, a ductile lower crust with density 1.32 g/cm^3 and viscosity 8.0×10^3 Pa s and an upper brittle crustal layer of sand mixed with $\sim$10% of ethyl-cellulose with density 1.3 g/cm^3 (Figure 3b). This stratified lithosphere overlaid the model asthenosphere, represented by honey, with density 1.5 g/cm^3 and viscosity 10^1 Pa s. The thickness of these layers is shown in Figure 3b. The reader is referred to *Davy and Cobbold* [1988, 1991] and *Brun* [2002] for a general treatment on the scaling of these materials.

[21] The rate of shortening affects the viscosity of the ductile layers, hence the degree of coupling between brittle and ductile layers. Faster deformation rates lead to a more distributed type of deformation [*Brun*, 1999]. Therefore the convergence velocity was empirically calibrated by comparing the fault spacing of the models with the one of the first-order faults in the Eastern Alps (Figures 1a and 1b). After testing shortening velocities of 0.25, 0.5, 1.0, and 10.0 cm/h (Table 1), we opted for a standard velocity of 1 cm/h.

[22] The models were confined along three sides by Plexiglas and only the fourth margin was deformable, consisting of silicone, whose viscosity and density were intermediate between those of the mantle and the lower crust. In the following we will refer to this margin as the eastern margin and to the others as northern, western, and

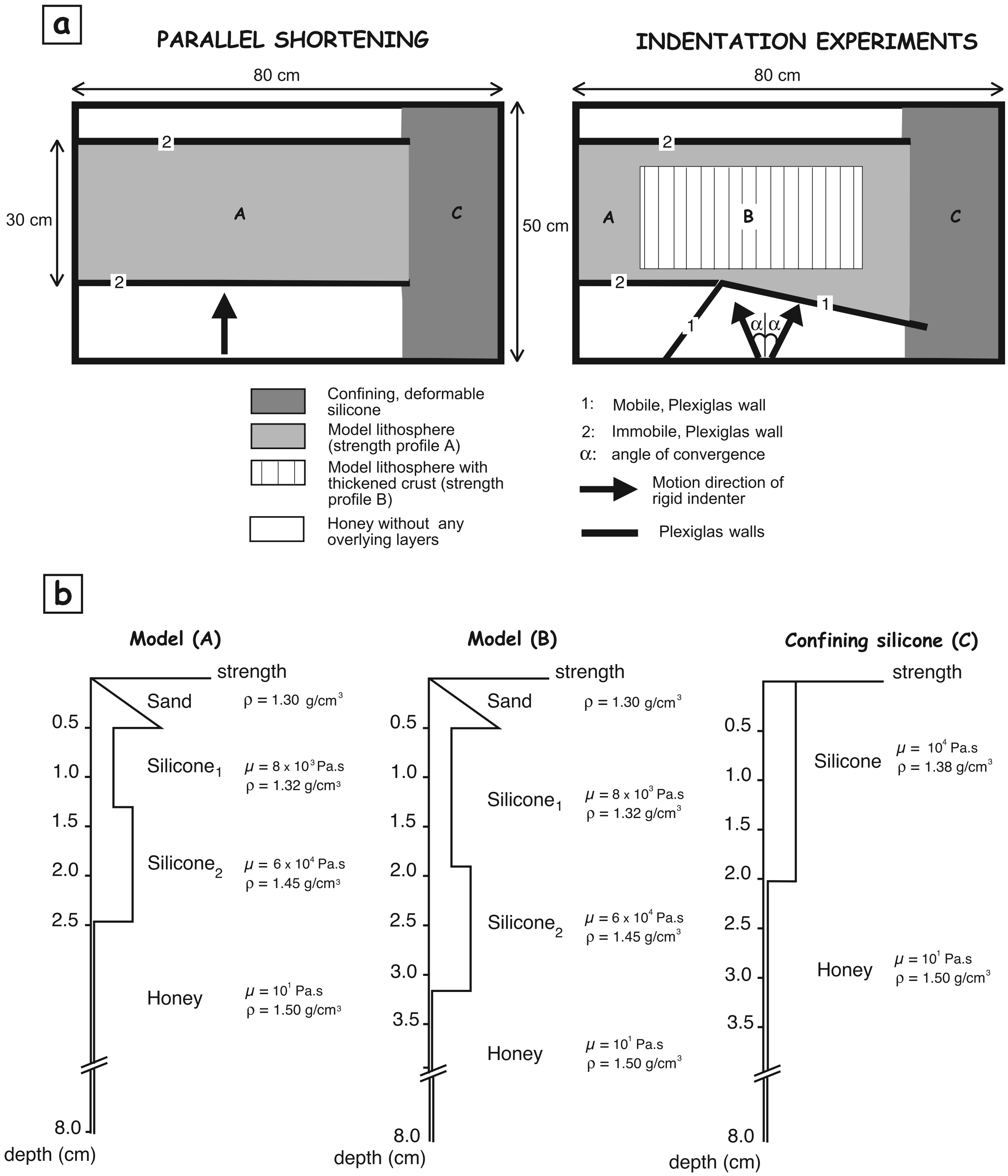

Figure 3. Schematic drawing of experimental set up and material rheologies. (a) Model geometry before deformation. (b) Strength-depth profiles and materials properties at room temperature. Capital letters refer to areas marked by the same letters in Figure 3a.

southern margins (Figure 3a). The Plexiglas walls were directly in contact with the silicone and sand layers, without a lubricating material along the interface. Therefore the mechanical coupling between rigid indenter and deformable model was rather strong.

[23] The effects of erosion and changing temperature were not taken into account in our experiments. These factors are expected to affect the long-term evolution of a fault system but not its nucleation pattern, which is the major object of our study.

Table 1. Boundary Conditions of Experiment

Experiment	Geometrical Configuration	Convergence Velocity, cm/h	Rheological Stratification[a]	Convergence Direction	Figure
01	Parallel plates	1	B UP - DC – BM - DM - A	N	no figure
02	Parallel plates	0.5	B UP - DC – BM - DM - A	N	no figure
03	Parallel plates	0.75	B UP - DC - DM - A	N	no figure
I	Parallel plates	1	B UP - DC - DM - A	N	Figure 4
II	Indenter on southern margin Surface of confining medium: 20 × 50 cm	1.0	B UP - DC - DM - A	N	Figure 5
III	Indenter on southern margin Surface of confining medium: 20 × 50 cm	1.0	B UP - DC - DM - A	N20°E	Figure 6
IV	Indenter on southern margin Surface of confining medium: 20 × 50 cm	0.25	B UP - DC - DM - A	N20°E	no figure
V	Indenter on southern margin Surface of confining medium: 20 × 50 cm	1.0	B UP - DC with doubled thickness - DM - A	N20°E	Figure 9
VI	Indenter on southern margin Surface of confining medium: 20 × 50 cm	10.0	B UP - DC with doubled thickness - DM - A	N20°E	no figure
VII	Indenter on southern margin Surface of confining medium: 20 × 50 cm	1.0	B UP - DC with doubled thickness - DM – A; low viscosity ($10^2 – 10^3$ Pa s), 2 mm thick layer on top of DC, in front of indenter	N20°E	no figure
VIII	Indenter on southern margin Surface of confining medium: 20 × 50 cm	1.0	B UP - DC - DM - A	N30°E	Figure 7
IX	Indenter on southern margin Surface of confining medium: 40 × 50 cm	1.0	B UP - DC - DM - A	N20°E	no figure
X	Indenter on southern margin Surface of confining medium: 20 × 50 cm	1.0	B UP - DC with doubled thickness - low viscosity ($10^2 – 10^3$ Pa s), 2 mm thick lower crustal layer - DM – A	N20°E	Figure 10
XI	Indenter on southern margin Surface of confining medium: 20 × 50 cm	1.0	Central area: B UP - DC with N20°E doubled thickness - DM – A Margins: B UP – DC – BM - DM - A	N20°E	Figure 11
XII	Indenter on southern margin Surface of confining medium: 20 × 50 cm	1.0	B UP - DC with doubled thickness - DM - A	N20°W	Figure 8

[a]B UP, brittle upper crust (sand); DC, ductile crust (silicone); BM, brittle mantle (sand); DM, ductile mantle (silicone); A, Asthenosphere (honey).

[24] The indenter geometry (Figure 3a, right) resembles the Dolomites indenter of the southern Alps (Figures 1a and 1b), with a long ESE striking northern margin and a shorter NNE striking western margin. The western border represents the sinistral, transpressive Giudicarie Fault [e.g., *Werling*, 1992], forming an angle of 75° with the northern border, resembling the dextral transpressive [*Polinski and Eisbacher*, 1992] Pustertal Fault (Figure 1). Minor complexities of the shape of the Dolomites indenter (Figure 1) were not taken into account. The use of a rigid indenter is also a simplification [*Ratschbacher et al.*, 1991a; *Robl and Stüwe*, 2005b], because the South Alpine indenter was affected by some shortening during Tertiary indentation [e.g., *Castellarin et al.*, 1987; *Doglioni and Bosellini*, 1987].

5. Experimental Results

[25] In order to test the effect of an indenter and its convergence obliquity on the deformation pattern of the indented lithosphere, a first series of experiments was performed without an indenter by shortening a model between two parallel rigid plates (Figure 3a, left). These experiments were compared with a second series of models shortened by an indenter (Figure 3a, right), with different convergence directions. We refer to the first series as parallel shortening and to the latter ones as indentation experiments.

[26] In the following discussion, we express the amount of lateral displacement simply by measuring the increase in E-W length of the model between the corner of the indenter and the eastern margin of the lithospheric model. This allows us to compare directly the experimental results with constraints on the amount of lateral displacements from studies of the Eastern Alps, estimated in the same way (Figure 2).

5.1. Parallel Shortening

[27] The model lithosphere was shortened by up to 50% between two parallel rigid plates in a N-S direction, perpendicular to the plate margins (Figure 4). This configuration was applied both on four-layer models, including a brittle upper mantle layer, and on three-layer models in which the mantle was entirely ductile (Table 1). Irrespective of the rheological layering, the amount of shortening, and the convergence velocity (Table 1), the model lithosphere

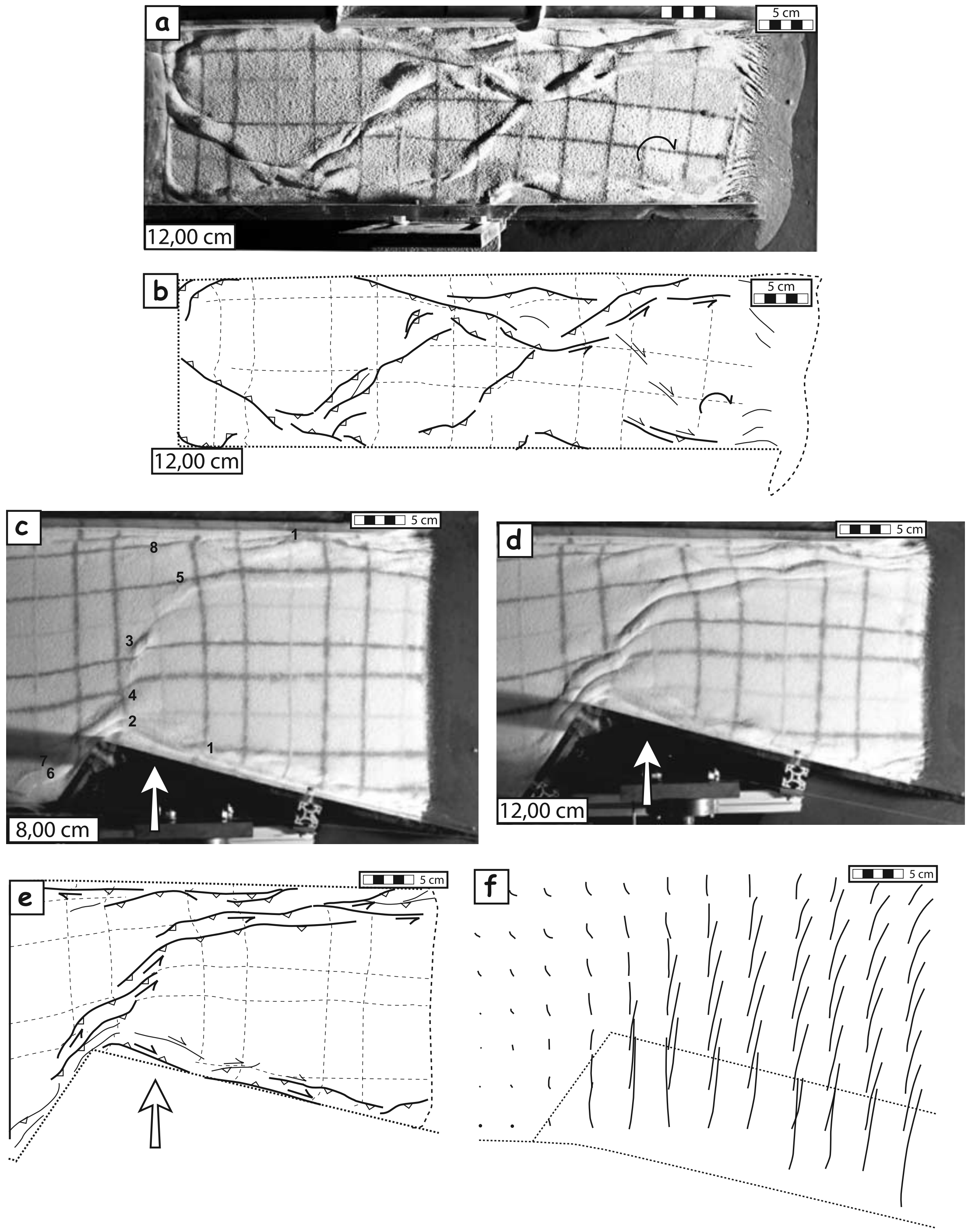

Figure 4. North directed convergence between rigid parallel plates (Figures 4a and 4b) and with a rigid indenter (Figures 4c, 4d, 4e, and 4f). (a) Surface of three-layer model (ductile upper mantle, ductile lower crust, brittle upper crust) shortened by 40% between parallel boundaries. Convergence direction was at 90° to the long side of the picture. Light gray and dark gray lines consist of colored sand, forming a grid, which enables the spatial distribution of deformation to be visualized. (b) Line drawing showing the major faults of Figure 4a. (c) Experiment II. Surface of three-layer model shortened northward by a rigid block whose shape reflects the Dolomites indenter after 26% (8 cm) of shortening. Numbers indicate the temporal sequence of nucleation of individual thrusts. (d) Surface of the model after 40% (12 cm) of shortening. (e) Line drawing showing the major faults of Figure 4d. (f) Particle flow paths calculated after 2, 4, 6, 8, 10, and 12 cm of shortening. Dashed lines indicate the margin of the indenter before the onset of deformation and at the end of the experiment.

shortened mainly by thickening along conjugate sets of thrusts striking at high angles to the convergence direction (Figures 4a and 4b). These thrusts nucleated after approximately 15% of shortening (Figure 4a) at an angle of 40–42° to the direction of shortening and rotated toward higher angles with increasing deformation (Figures 4b and 4c). E-W extension never exceeded a few percent, as also shown by the homogeneously distributed, consistent northward motion of solid marker particles (Figure 4d). Only in the final stages of shortening and in the immediate vicinity of the eastern margin of the model did the particle motion deviate slightly to the NNE (Figure 4d).

5.2. Indentation Experiments

[28] The mobile Plexiglas plate was replaced by a rigid indenter (Figure 3a). The convergence direction of the piston was changed from NNW directed (N20°W), to perpendicular (north directed), to oblique (N20° to 30°E).

5.2.1. North Directed Convergence (Experiment II)

[29] Shortening was initially accommodated by margin parallel thrusts along the northern and southern borders of the model (numbered 1 in Figure 4c). These thrusts can probably be regarded as a boundary effect of the model. Additional deformation localized along a fold-and-thrust belt, crosscutting the model from its northeastern border to the corner of the indenter (Figures 4c and 4d). This structure formed as a series of en echelon thrusts (Figure 4c) that propagated from the indenter corner northward, although some out-of-sequence thrusts also developed (number 4 in Figure 4c). The individual thrusts formed at an angle of ~30° to the convergence direction (Figure 4c), and rotated clockwise with increasing deformation, attaining an angle of ~60° with the convergence direction (Figures 4d and 4e) by the end of the experiment.

[30] The number of margin-parallel thrusts (Figures 4c, 4d, and 4e) accommodating a component of lateral displacement increased during convergence. Dextral strike slip occurred adjacent to the long side of the indenter and sinistral strike slip occurred along the northern margin of the model (Figures 4c, 4d, and 4e). These structures, together with the en echelon thrusts, delimited a large wedge of nearly undeformed material which escaped eastward. However, the amount of lateral displacement was very small (~3%). Hence the divergent geometry of the rigid plates due to the use of the angled orogenic indenter did not increase the amount of lateral displacement compared to the parallel-shortening experiments.

[31] The particle displacement paths east of the leading edge of the indenter (Figure 4f) show a small component of eastward motion which increases slightly toward the northeastern part of the model at higher amounts of convergence, as shown by the increasing eastward curvature of the particle paths, from south to north (Figure 4f). The en echelon thrust belt described above separates an area with north to NNW directed displacement in the north from an area with north to NNE directed displacement in the south (Figure 4f). This is consistent with a component of sinistral displacement along the thrust belt. To the west of the indenter edge, particle displacements are much shorter and directed to the NNW or NW (Figure 4f). Therefore the particle paths in front of the leading edge of the indenter were divergent, causing a small (~ 15%) amount of E-W extension in this area.

5.2.2. N20°E Directed Convergence (Experiment III)

[32] Oblique convergence of the indenter at an angle of 20° toward the NNE initially localized deformation (after 5 to 10% of shortening) in a series of in-sequence thrusts adjacent and subparallel to the northern border of the indenter (numbers 01, 02 in Figure 5a). These structures also accommodated a small component of dextral displacement, especially at the eastern margin of the indenter. With increasing amounts of convergence (14 to 40% shortening), deformation propagated both northward and eastward from the indenter edge, forming a complex fault pattern (Figures 5a and 5b) which consisted of subparallel sets of thrusts showing three different orientations: NW striking, NE striking, and E-W striking (Figures 5a and 5b). The NW striking thrusts also accommodated a minor component of dextral lateral displacement, and the NE striking thrusts a minor component of sinistral displacement. Nucleation started with two NW striking thrusts (numbered 1 and 2 in Figure 5a), but no simple spatial trend could be recognized in the sequence of nucleation of the following thrusts (numbered 3 to 12 in Figure 5a). The wedge-shaped area of deformation escaped to the east, by an amount which gradually increased southward (Figure 5a) and experienced an anticlockwise rotation (Figure 5a). The maximum amount of E-W extension attained by this wedge is less than 20% (Figure 5a), although E-W extension locally reaches 60–70% in front of the indenter corner, as indicated by the increased southward stretching of the dashed line in Figure 5a.

[33] The displacement field (Figure 5c) shows NNE directed particle motion during the first increments of shortening (0 to ~34%), gradually changing to north directed displacement during the final increments of shortening (~34–46%). The small displacement of particles adjacent to the western indenter margin was north to NNW directed (Figure 5c), hence strongly deviating from the imposed NNE convergence. As a consequence, the area in front of the leading edge of the indenter separates a wedge moving to the NNE from the western part of the model, which remains nearly undeformed (Figure 5a). This differential displacement resulted in a component of E-W extension (Figure 5a). However, the most pronounced eastward motion occurred at the eastern end of the model, not in front of the indenter corner (Figure 5c). Therefore extension in front of the indenter edge did not result from an orogen-parallel, east directed flow, but from the differential and locally divergent flow of particles on both sides of the indenter corner (Figure 5c).

[34] Compared to the indentation experiment with north directed convergence, the particle displacement field in Figure 5c shows a less distributed, wedge-shaped area of displacement in front of the indenter. The northern margin of this wedge is characterized by NE directed displacement paths (Figure 5c), flanking north, to NNW directed paths further north (Figure 5c). This displacement discontinuity

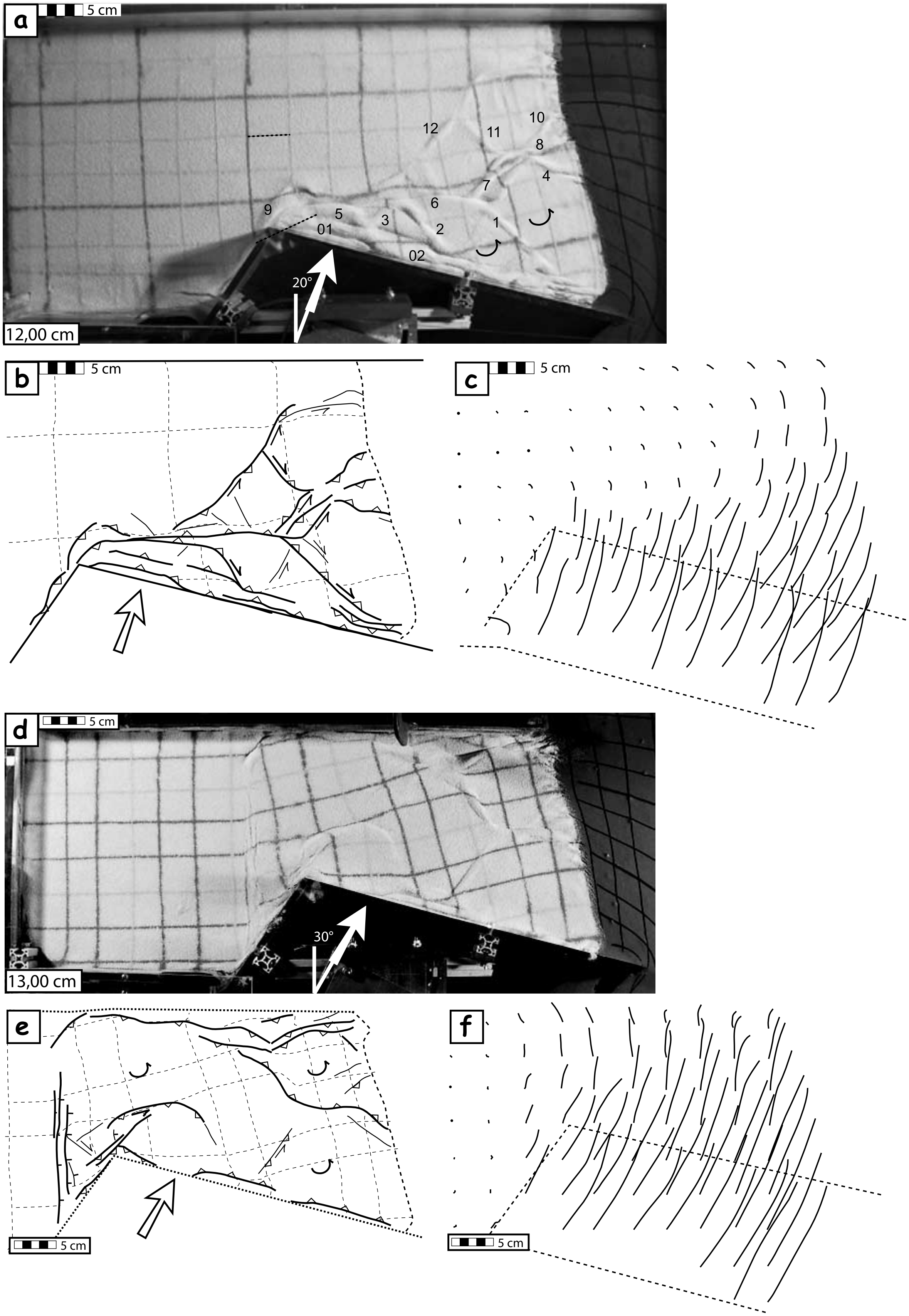

Figure 5

marks the sinistral faults (Figure 5b), which drive the eastward motion of the deformed wedge.

5.2.3. N30°E Directed Convergence (Experiment VIII)

[35] Oblique convergence with an angle of 30° toward the NNE resulted in a fault pattern dominated by E-W to ENE striking thrusts, mainly located close to the northern and southern boundaries of the model (Figures 5d and 5e). Some of these thrusts were also affected by sinistral lateral displacements, but no dextral strike-slip deformation was observed (Figures 5d and 5e).

[36] Pronounced E-W extension developed in front of the indenter edge (Figure 5d) and increased to the west, where it localized in a series of N-S striking normal faults (Figures 5d and 5e). These faults separate the western part of the model that did not suffer any deformation, from the eastern part, which was shortened and rotated up to 20° anticlockwise (Figure 5d). In contrast to the other experiments, rotation affected the entire eastern half of the model, from its northern margin to the indenter. The vertical axis of rotation was located at the northern boundary of the model (Figure 5d), thus inducing progressively larger displacements toward the south and a gradual southward increase in the amount of lateral displacement. At the southern margin of the indenter, E-W extension exceeded 20%.

[37] The pattern of particle displacement paths (Figure 5f) shows a gradual change from NNE directed motion in front of the long margin of the indenter, to north directed motion in the northernmost part of the model. These paths delimit a wedge-shaped area between the northern margin of the model and the leading edge of the indenter (Figure 5f). The discontinuity in the direction of particle motions along the southern boundary of this wedge points to a sinistral component of displacement, which however is not associated to one single, continuous fault (Figures 5d and 5e), as observed in the previous experiments. In front of the western margin of the indenter a continuous change of motion from NNE directed in the south to north directed further north reflects the progressive northward decrease in E-W extension observed in Figure 5d.

5.2.4. N20°W Directed Convergence (Experiment XII)

[38] Oblique convergence with an angle of 20° to the NW shows a very different fault pattern (Figures 6a and 6b) than in the experiments described above. With the exception of a long thrust fault that formed adjacent and parallel to the northern margin of the model (Figures 6a and 6b), deformation was strongly localized in the immediate vicinity of both margins of the indenter. In front of the western side of the indenter, a series of en echelon thrusts evolved into tight folds, which wrapped around the indenter edge. In this area, shortening was transferred eastward into E-W striking thrusts, which also accommodated a significant dextral displacement (Figures 6a and 6b). The amount of dextral strike slip immediately in front of the long margin of the indenter progressively decreased toward the east, as shown by the offset of the vertical markers (Figure 6a). Only in the very late stages of convergence (>30% shortening, Figures 6a and 6b) did faults propagate into the central part of the model, forming conjugate sets of NW striking and SE striking transpressive thrusts, which accommodated sinistral and dextral displacements, respectively (Figures 6a and 6b). The late appearance of these conjugate structures, which in most of the other experiments formed in the early stages of deformation, is due to the fact that shortening in front of the ESE striking margin of the indenter is much smaller if convergence is NW directed instead of NNE directed. E-W extension in front of the leading edge of the indenter was small (Figures 6a and 6b).

[39] Despite the NNW directed convergence, a significant component of displacement toward the NE affected the eastern half of the model (Figure 6c). Nevertheless, the amount of E-W extension was small (<5%) and less than in the NNE directed experiments.

[40] The displacement pattern (Figure 6c) shows a very gradual transition from NE directed motion in the east, to north directed motion in front of the indenter edge, to NW directed motion in the west (Figure 6c). A discontinuity occurs in front of the long side of the indenter, where particles moved parallel to the imposed NNW direction, but rapidly changed toward a NE direction further north. This discontinuity is expressed by the dextral transpressive faults observed in front of the indenter (Figures 6a and 6b). The progressive change from NW to NE directed motion of the southernmost particles of the model (Figure 6c) explains the eastward decrease in the amount of dextral motion described above. The transition from north directed to NE directed motion from east to west, respectively (arrows in Figure 6c), resulted in a component of E-W extension, as also shown by the deformation of the grid (Figure 6a).

5.3. Indentation Experiments With Changes of Crustal Thickness and Rheology

[41] The following experiments were conducted with the same geometrical boundary conditions used in the previous indentation experiments, but with different rheological

Figure 5. Oblique indentation at 20° toward the NNE (experiment III, Figures 5a, 5b, and 5c) and 30° toward the NNE (Figures 5d, 5e, and 5f, experiment VIII). (a) Experiment III. Surface of three-layer model shortened "obliquely", at 20° toward the NNE after 40% (12 cm) of shortening. Dashed lines are reference lines, showing increased E-W extension in front of the indenter corner; numbers indicate the nucleation sequence of individual thrusts. (b) Line drawing showing the major faults of Figure 5a. (c) Particle flow paths calculated after 2, 4, 6, 8, 10, 12, 14, and 16 cm of shortening. Dashed lines indicate the margin of the indenter before the onset of deformation and at the end of the experiment. (d) Experiment VIII. Surface of three-layer model shortened "obliquely," at 30° toward the NNE, after 40% (12 cm) of shortening. (e) Line drawing showing the major faults of Figure 5d. (f) Particle flow paths calculated after 2, 5, 7, 9, 11, 13, and 15 cm of shortening.

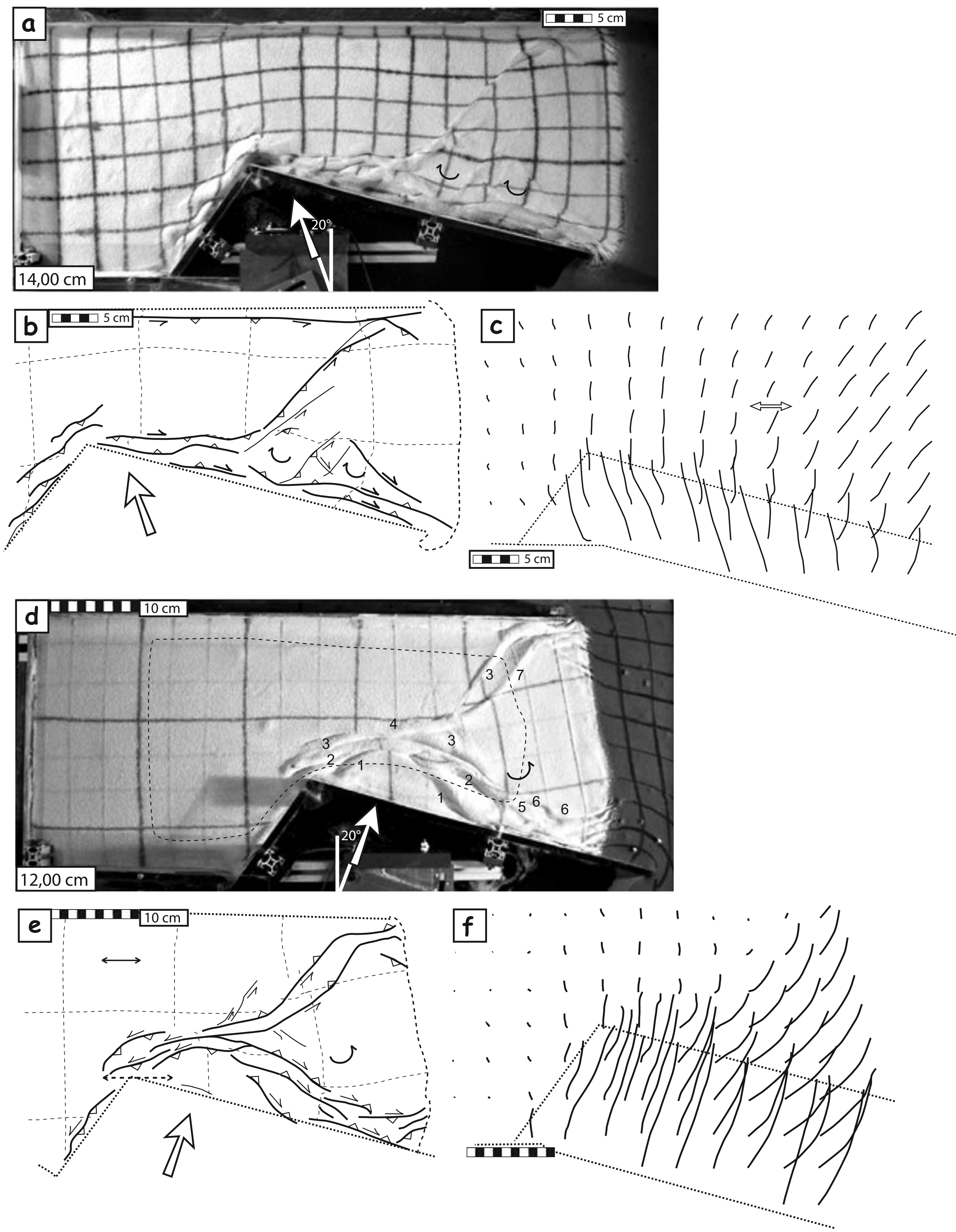
a
5 cm
20°
14,00 cm
b
5 cm
c
5 cm
d
10 cm
3
7
4
3
3
2
1
2
1
5
6
6
20°
12,00 cm
e
10 cm
f

Figure 6

layering. The convergence direction of the indenter was always N20°E.

5.3.1. Thickened Ductile Crust (Experiment V)

[42] The thickness of the ductile crust was doubled (1.5 instead of 0.75 cm) in the central part of the model (dashed line in Figure 6d). In contrast to experiment III (Figure 5a), which was shortened in the same direction, but had a thinner ductile crust, deformation rapidly propagated from the indenter margin northward, localizing along sets of conjugate transpressive thrust belts (Figures 6d and 6e). NW and NE striking thrusts also accommodated dextral and sinistral strike-slip displacement, respectively. The thrusts nucleated in sequence, from the indenter margin northward (numbers in Figure 6d). After a large amount of shortening (~32%) deformation also propagated eastward. With further shortening, the conjugate pairs of NE and NW striking thrusts evolved into tight folds, which formed an arcuate fold belt in front of the ENE striking margin of the indenter (Figures 6d and 6e).

[43] Significant E-W extension, of up to 100%, affected the area in front of the indenter edge (Figure 6d), as shown by the increasing distance between the vertical marker lines (Figure 6d). Another area characterized by distributed E-W extension was located at the eastern margin of the arcuate structure (Figure 6d). Still further to the east, extension was transferred into eastward diverging, transpressive faults, bounding a large and nearly undeformed wedge (Figures 6d and 6e) that escaped eastward, as observed in experiment III (Figure 5a). The maximum amount of E-W extension of the bulk model almost attained 20%.

[44] The particle displacement field (Figure 6f) shows some similarities with that of experiment III (Figure 5c) which was also shortened to the NNE, but had a ductile crust of normal thickness. Both displacement fields show that the deformed area wedges out from east to west, close to the indenter edge, and both displacement fields show an increase in the eastward component of particle displacement from east to west. However, experiment V shows a stronger partitioning of displacement into NE directed motion in the eastern part of the model and north directed motion in the central part (Figure 6f). E-W extension occurred at the transition between these two areas in order to maintain compatibility between the eastward escaping wedge and the arcuate belt that was undergoing N-S shortening.

5.3.2. Decoupled Crust-Mantle Boundary (Experiment X)

[45] In this experiment (Figure 7a), the lithospheric model was prepared by adding a thin (2mm thick) and low-viscosity (1.0×10^3 Pa s) layer at the base of the ductile crust, hence reducing the mechanical coupling between ductile crust and ductile mantle, compared to the experiments above. Similar boundary conditions were shown to enhance lateral extrusion in thermomechanical finite element models [*Seyferth and Henk*, 2004]. Localization of deformation occurred after greater shortening than in the experiments described above, along faults that were mainly located in the central part of the model (Figures 7a and 7b). In spite of the lower crustal weakness added to this model, the amount of E-W extension was not larger than in the previous experiments (Figure 7a).

[46] Except for the area located north of the leading edge of the indenter, the particle motion is very close to the imposed convergence direction (Figure 7c), and any deviations from this direction are smooth and distributed over large areas (Figure 7c). E-W extension occurred in front of the indenter edge (Figure 7a), but this extension was modest, as shown by the subparallel orientation of particle paths on both sides of the indenter edge (Figure 7c).

5.3.3. Orogen-Parallel, Lithospheric Weak Zone (Experiment XI)

[47] The lithospheric model was constructed with a built-in, E-W striking weak zone in the central area (Figure 7d), as previously performed by *Willingshofer et al.* [2005]. This weak zone along the central axis of the orogen should simulate a thermally weakened corridor in the area of maximum thickening. The weak zone consisted of an upper brittle crust, a ductile lower crust and a ductile mantle layers (Table 1). It was surrounded by a stronger lithosphere, containing a brittle upper mantle (sand) in addition to the latter three layers.

[48] The localization pattern of this model differed strongly from the previous ones. During the initial stages of shortening, deformation localized within, and close to the area of the built-in weakness zone, particularly along its boundaries. Only during the later stages of shortening did the deformation propagate toward the indenter margin (Figures 7d and 7e). The conjugate thrusts observed in experiments III and V did form in this model too, but they were mostly located along the margins of the orogen-parallel weak zone. Therefore their orientation was close to the long axis of the model, even in the initial phases of propagation.

[49] At the end of deformation (46% shortening, Figures 7d and 7e), the eastern margin of the model did not show any deflection in the eastward continuation of the

Figure 6. Oblique convergence at 20° to the NNW (experiment XII, Figures 6a, 6b, and 6c) and 20° to the NNE (experiment V, Figures 6d, 6e, and 6f). (a) Surface of three-layer model shortened "obliquely," at 20° toward the NNW after 46% (14 cm) of shortening. (b) Line drawing showing the major faults of Figure 6a. (c) Particle flow paths calculated after 2, 5, 7, 9, 11, 13, and 15 cm of shortening. Open arrows indicate area of distributed E-W extension. (d) Experiment V, modified after *Rosenberg et al.* [2004]. Surface of three-layer model shortened "obliquely," at 20° toward the NNE, after 40% (12 cm) of shortening. Lower crustal thickness in the central part of the model is doubled. Dashed line indicates the margin of the area with doubled thickness of the lower crust. (e) Line drawing showing the major faults of Figure 6d. Solid E-W line with arrowheads indicates the original length of the line, which is dashed, in front of the indenter corner. (f) Particle flow paths calculated after 2, 4, 6, 8, 10, 12, 14, and 16 cm of shortening.

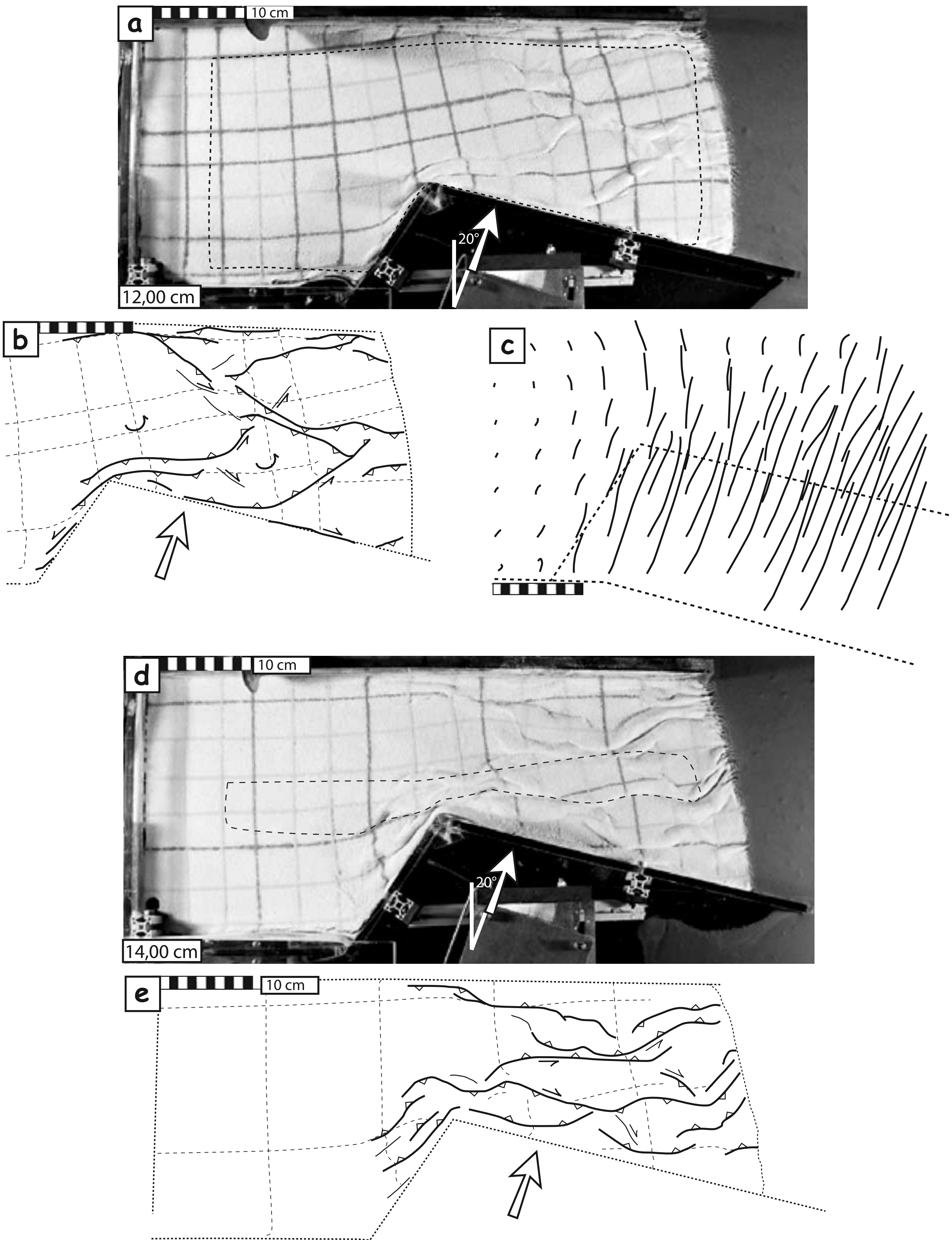

Figure 7

weak zone, indicating that the latter rheological heterogeneity did not increase the ability of the model to move laterally.

5.3.4. Larger Size of the Area Accommodating Lateral Displacement (Experiment IX)

[50] One experiment was conducted with a larger area of confinement, i.e., by setting the indenter further west, hence increasing the surface of the laterally confining material in the east. Instead of a surface of 17 × 50 cm (C in Figure 3b) as in the models above, the eastern confinement had an area of 35 cm × 50 cm, hence the eastern margin of the indenter was twice as far from the eastern border of the Plexiglas box (Figure 3) compared to all experiments described above. As a consequence, thickening of the confining medium during shortening of the model was less than in the other experiments, potentially allowing for easier lateral motion. However, there was no increase in the amount of E-W extension compared to the other experiments.

6. Discussion

6.1. Similarities Between the Experiments and the Eastern Alps

[51] The greatest similarities between the deformation pattern of the Eastern Alps and those of our models are observed in the NNE directed experiment V (Figure 6d). These similarities were discussed by *Rosenberg et al.* [2004] and can be summarized as follows: (1) the tight folds in front of the leading edge of the indenter (Figure 6d) are analogous to the Ahorn, Tux, and Zillertal antiforms of the western Tauern Window (Figure 1b), and to the Sonnblick and Hochalm domes of the eastern Tauern Window (Figure 1b); (2) the folds of the model are associated with sinistral displacements in the west and dextral motion in the east (Figures 6d and 6e); the same is true in the Tauern Window, where the western and eastern antiforms are separated by sinistral and dextral strike-slip faults, respectively (Figure 1b); (3) the axial planes of the folds in the western and eastern parts of the dome form an angle of ~120° to each other, both in the model (Figures 6d and 6e) and in the Tauern Window (Figures 1a and 1b); (4) a triangular, nearly undeformed region occurs between the northern margin of the indenter and the folded region (Figures 6d, 6e, and 8), as also observed between the Pustertal Fault and the DAV Fault (Figure 1b); (5) an area of pronounced east-west extension coinciding with the western part of the folded region characterizes both the model (Figure 6d) and the western margin of the Tauern Window (Brenner extensional fault; Figures 1a and 1b); (6) a second area characterized by E-W extension, but less intense than the latter one is found at the eastern margin of the NW striking thrusts and folds (Figure 6d), as also observed along the Katschberg extensional fault in the Eastern Alps (Figures 1a and 1b); (7) a series of northeast and southeast striking transpressive faults with sinistral and dextral displacements, respectively, transferred east-west extension from the arcuate fold zone to the eastern boundary of the model, inducing a modest amount of lateral extrusion (Figures 6d and 6e). These structures are analogous to the sinistral SEMP and Mürz-Murtal faults and to the dextral Mölltal Fault (Figures 1a and 1b); (8) the western margin of the indenter is bordered by a thrust belt, which also accommodates a sinistral displacement (Figures 6d and 6e); and (9) the eastern part of the model underwent counterclockwise rotation (Figures 6d and 6e), as documented by paleomagnetic studies east of the Tauern Window [*Márton et al.*, 2000].

[52] NNW directed convergence of the rigid indenter resulted in dextral shearing and shortening along its northern margin (Figures 6a and 6b), as observed in the Eastern Alps along the Pustertal Fault (Figures 1a and 1b). Another similarity between model and nature is the occurrence of distributed E-W extension in the model (open arrow in Figure 6c) in an area that might correspond to the Katschberg extensional Fault in the Eastern Alps (Figures 1a and 1b). However, most of the remaining structures strongly differ from those of the Tertiary Eastern Alps: (1) some E-W oriented extension takes place in front of the indenter edge, as shown by the greater distance between vertical markers lines in Figure 6a, but only to a limited extent, not comparable to that of experiments with NNE directed shortening; (2) the very pronounced shortening along the western margin of the indenter, accommodated by tight en echelon thrusts and folds adjacent to this margin (Figures 6a and 6b) is not known in the western margin of the indenter in the Alps (Figures 1a and 1b), where Tertiary exhumation was rather small; (3) E-W striking dextral faults formed in front of the indenter corner in the model (Figures 6a and 6b), whereas this area is dominated by sinistral shearing in the Eastern Alps (Figure 1b); (4) sinistral faults bounding the northern side of the extruding wedge, analogous to the SEMP Fault (Figure 1b) in the Alps, only formed in the very late stages of these experiments (Figures 6a and 6b) and accommodated only minor offsets; and (5) the area in front of the long side of the indenter margin rotated

Figure 7. Oblique convergence at 20° to the NNE with weak layer at the mantle/lower crust boundary (experiment X, Figures 7a, 7b, and 7c) and with weaker channel in the central part of the model (experiment XI, Figures 7d and 7e). (a) Surface of four-layer model shortened "obliquely," at 20° toward the NNE, after 40% (12 cm) of shortening. In addition to the three layers of the previous experiments, this model contains a thin and very weak lower crustal layer, directly on top of the ductile mantle. Dashed line indicates the position of the low-viscosity layer at the beginning of deformation. (b) Line drawing showing the major faults of Figure 7a. (c) Particle flow paths calculated after 2, 4, 6, 8, 10, 12, 14, and 16 cm of shortening. (d) Surface of experiment XI, after 46% of shortening. The model lithosphere consists of four layers with an orogen-parallel weak (three-layer) zone in the central area of the model. Dashed line indicates the initial position of the three-layer weakness build in the initial model. (e) Line drawing showing the major faults of Figure 7d.

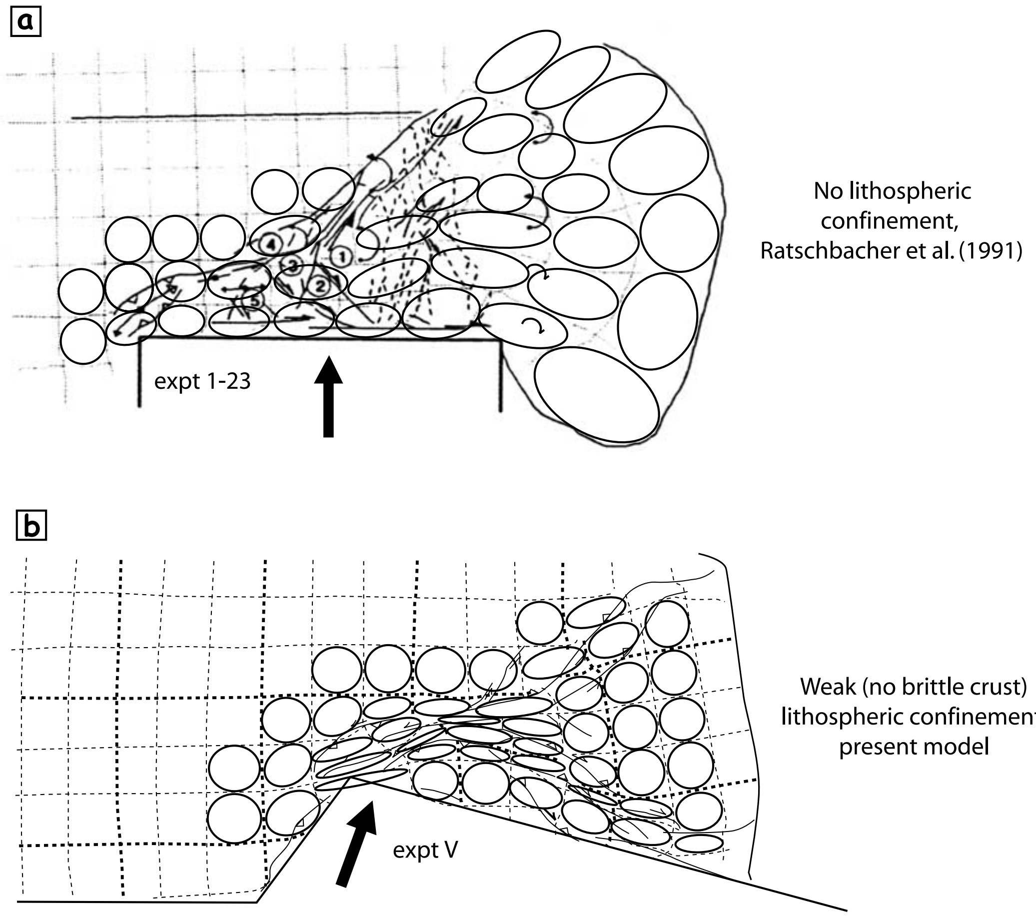

Figure 8. Comparison of the distribution of deformation in previous and present models. Within each deformed square of the surface grid, we plotted an ellipse that best represents the deformed square. Note, however, that deformation of most grid squares was not homogeneous. Therefore ellipses can only be regarded as a rough visualization of surface strain within each deformed square. Moreover, the ellipses represent a nearly horizontal section through the deformation ellipsoids, whose major axes are not necessarily within the plane of the figure. (a) Deformed grid of model 1-23 by *Ratschbacher et al.* [1991a]. (b) Experiment V of the present work, after 12 cm of shortening.

clockwise, not anticlockwise as inferred for the Eastern Alps from paleomagnetic results [*Márton et al.*, 2000].

[53] North directed convergence concentrated shortening in a fold and thrust belt striking across the entire model at a high angle to the northern indenter edge (Figures 4d and 4e) and in the continuation of the western indenter margin. Only after large amounts of shortening (Figure 4d) did this structure rotate into an ENE strike at the northern margin of the model, where it accommodated small amounts of sinistral shearing (Figures 4d and 4e). Such a structure is not known from the Eastern Alps (Figures 1a and 1b). Dextral shearing took place along the northern indenter margin, as along the Pustertal fault in the Eastern Alps. The lithospheric wedge bounded by this fault and the northernmost part of the aforementioned sinistral fault remained virtually undeformed (Figure 4d) and suffered minor dextral rotation, in contrast to the anticlockwise rotation inferred for the Eastern Alps [*Márton et al.*, 2000]. This model did not show any significant amount of E-W extension in front of the indenter edge (Figure 4d), in the area corresponding to the Brenner extensional fault in the Eastern Alps.

[54] N30°E directed convergence resulted in a set of N-S striking extensional faults (Figures 5d and 5e) in front of the western margin of the indenter. These structures do recall the kinematics and strike of the Brenner fault in the Alps (Figures 1a and 1b) but were located further west with respect to the indenter edge. Dextral shearing along the northern indenter margin, i.e., corresponding to the dextral Pustertal Fault (Figures 1a and 1b), was not observed (apparent dextral displacement of some markers adjacent to the northern indenter margin in Figure 5d was due to thrusting oblique to the markers, not to dextral shearing). A sinistral fault corresponding to the SEMP Fault (Figures 1a and 1b) was only poorly defined above the indenter edge. Sinistral rotation of the eastern part of the model and E-W

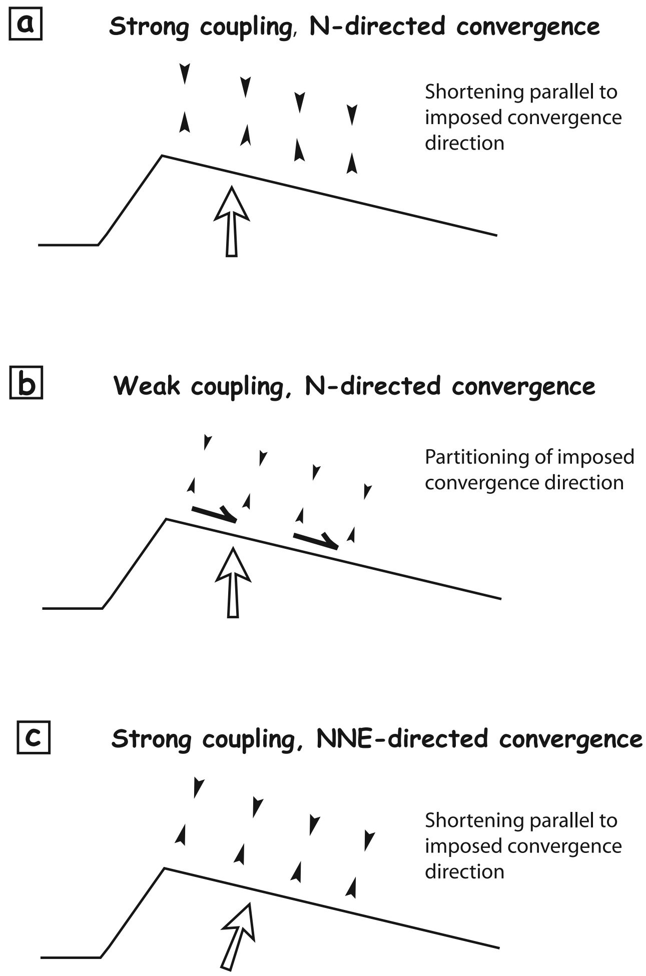

Figure 9. Schematic sketch showing the possible effect of strong and weak coupling on the deformation pattern resulting from one convergence direction. (a) North directed convergence and strong mechanical coupling between indenter and indented lithosphere. (b) North directed convergence and weak coupling. (c) NNE directed convergence and strong coupling. In situations in Figures 9b and 9c, similar structures are expected north of the indenter contact.

extension in front of the indenter edge were very pronounced (Figures 5d), as inferred for the Eastern Alps.

6.2. Counterclockwise Rotation in the Models and in the Eastern Alps

[55] Counterclockwise rotation of the Eastern Alps [*Márton et al.*, 2000] has been explained as the consequence of dextral motion along the southern margin of the eastward escaping wedge (Pustertal Fault; Figure 1) that was larger than the sinistral motion bounding the northern margin of the wedge (SEMP Fault; Figure 1). Previous indentation experiments (e.g., *Ratschbacher et al.*'s [1991a] experiment 6) did result in a sinistral rotation of the eastern Alpine wedge due to larger dextral displacements along the indenter margin, compared to sinistral displacement along the NE striking wedge boundary further north. To obtain these displacements, their experiment was carried out with a north motion of a SE striking indenter [*Ratschbacher et al.*, 1991a], hence increasing the amount of dextral displacement during N-S shortening. However, the orientation of the South Alpine indenter is ESE to E-W, and all experiments performed with similarly oriented indenters did not induce sinistral rotations in the indented model [*Ratschbacher et al.*, 1991a].

[56] In our experiments, anticlockwise rotation was obtained by imposing an oblique, NNE oriented convergence direction on an ESE oriented indenter, as in the Eastern Alps. Sinistral rotation in these models was due to a gradient in the amount of NE directed displacements, large in the vicinity of the long margin of the indenter and decreased northward (Figures 5a and 6d), attaining zero displacement at the northern margin of the model (Figures 5a and 6d).

6.3. Effect of Indenter Convergence Direction on the Experimental Deformation Patterns: Implications for the Eastern Alps

[57] Our models showed that small changes in the obliquity of the indentation direction with respect to the plane of collision result in very different patterns of deformation (compare Figures 4d, 5a, 5d, and 6a) and that the closest similarity to the fault pattern of the Eastern Alps is obtained when convergence is oriented with 20° to the NNE (Figures 5a and 6d). Interestingly, this orientation is consistent with the displacement inferred from present-day surface velocities calculated with respect to Eurasia [*Grenerczy et al.*, 2005]. All experiments conducted with convergence directions other than 20° to the NNE showed some major differences with the deformation pattern of the Eastern Alps.

[58] The fault pattern resulting from a specific convergence direction depends largely on the degree of mechanical coupling between the rigid indenter and the deformable lithospheric model. Experiments III and V are both characterized by a close similarity between the imposed NNE direction of indentation and the particle displacement in front of the long side of the indenter. The same is true for experiment II, where the N-S convergence direction of the indenter is subparallel to the displacement of material particles in the deformed lithospheric model (Figure 4f). These observations point to a strong mechanical coupling between indenter and deforming model with our boundary conditions (Figure 9a). However, one could imagine a situation in which indenter and indented block are weakly coupled due to the presence of a weak fault along their contact. Indeed, this scenario has been proposed by *Handy et al.* [2005] for coaxial exhumation of the Tauern Window and coeval dextral displacement along the Pustertal Fault. Under these conditions a north or even NNW directed convergence of the indenter could be partitioned into a significant dextral strike-slip component along the northern indenter margin (Figure 9b), thereby leading to a deviation of material particles from a north directed to a NNE directed path. Hence the type of structures observed in models III and V (Figures 5a and 6e) may be obtained by moving the indenter to the north instead of NNE if the plane of contact

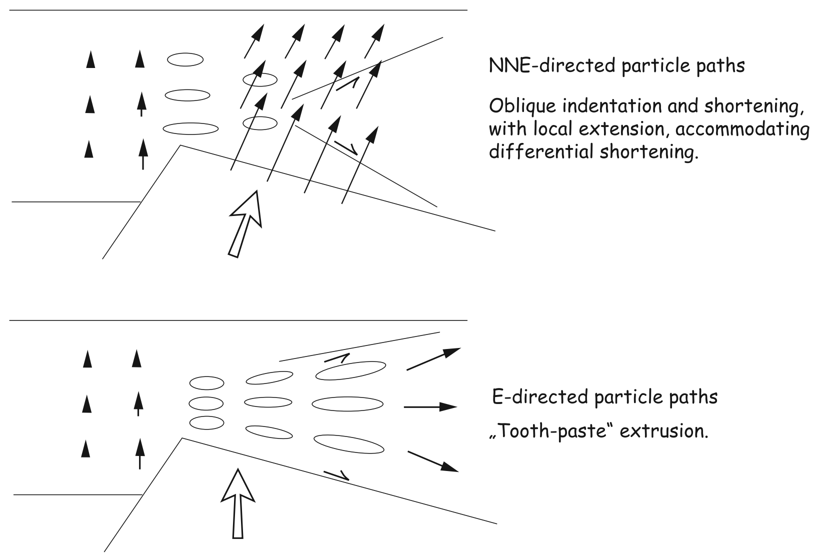

Figure 10. Schematic drawing illustrating the particle paths and the spatial distribution of E-W extensional deformation in the present, NNE directed models, and in a "toothpaste" tectonic model.

between indenter and indented lithosphere was sufficiently weakened (Figure 9).

6.4. Lateral Displacement

[59] In line with previous studies [*Davy and Cobbold*, 1988, 1991; *Ratschbacher et al.*, 1991a], the amount of lateral displacement in our laterally confined experiments was modest, even though the confining medium was weaker than the indented model lithosphere. Changing the boundary conditions from shortening between parallel plates (Figure 4a) to shortening between plates diverging toward the confining medium (e.g., Figure 4d) was not sufficient to increase the amount of lateral displacement, if the shortening direction was perpendicular to the northern boundary of the model (Figure 4d). In order to obtain large amounts of lateral displacements, previous authors performed some experiments confining the model lithosphere only with honey, i.e., the analogue asthenosphere [*Davy and Cobbold*, 1988, 1991; *Ratschbacher et al.*, 1991a]. Indeed, these experiments showed that lateral displacement can easily exceed 50% (note however, that the absolute value also depends on the amount of shortening and aspect ratio of the models). However, these boundary conditions are geologically unrealistic, because they simulate a continent confined by an asthenospheric layer that entirely lacks an overlying lithosphere. Under these conditions, the continent spreads laterally toward the asthenospheric layer, generating a deformation pattern characterized by the progressive increase of extension from west to east, as shown by the increasing length of the ellipses in Figure 8a. This deformation pattern is similar to that of spreading-gliding nappes [*Brun and Merle*, 1985]. Note that these boundary conditions lead to lateral displacements even in the absence of any shortening by the indenter. In contrast, the spatial distribution of deformation in the Tertiary Eastern Alps shows that E-W extension along an E-W traverse is nearly constant (e.g., in the North Calcareous Alps, Figure 2a) or increases westward, as in the central Eastern Alps (Figure 2). This deformation pattern is consistent with one of our experiments, in particular experiment V (Figure 8b), showing significant E-W extension in front of the indenter edge, but nearly zero extension at the eastern end of the model (Figure 8b). In the light of our reassessment of the amount of orogen-parallel extension in the Eastern Alps, suggesting no more than 20% (Figure 2), the amount of lateral displacement in some of the NNE directed experiments (e.g., experiment V, Figure 6d) is comparable to that of the Eastern Alps. Some 20% E-W extension were attained by displacing particles toward the NNE, not by the east directed particle motion (Figure 10) inferred from "toothpaste" tectonic models that have been applied to the Eastern Alps [*Meissner et al.*, 2002].

[60] Irrespective of the convergence direction, all models performed with an indenter resulted in conjugate sets of transpressive faults, with dextral strike slip at the southern margin of the model, and sinistral strike slip further north, as observed in the Eastern Alps, between the dextral Pustertal Fault in the south and the sinistral SEMP Fault further to the north (Figure 1). In contrast, these conjugate faults which accommodated the eastward displacement of a lithospheric wedge were only poorly developed (e.g., Figures 4a and 4b) or not present at all in the "parallel shortening" models, suggesting that nucleation of these faults was primarily due to the presence of the indenter. Indeed, the overwhelming majority of previous indentation experiments performed on a model lithosphere with moderate confinement or no confinement on one side, and a rigid confinement on the opposite side [*Tapponnier et al.*, 1982; *Davy and Cobbold*, 1988, 1991; *Peltzer*, 1988; *Peltzer and Tapponnier*, 1988; *Ratschbacher et al.* 1991a;

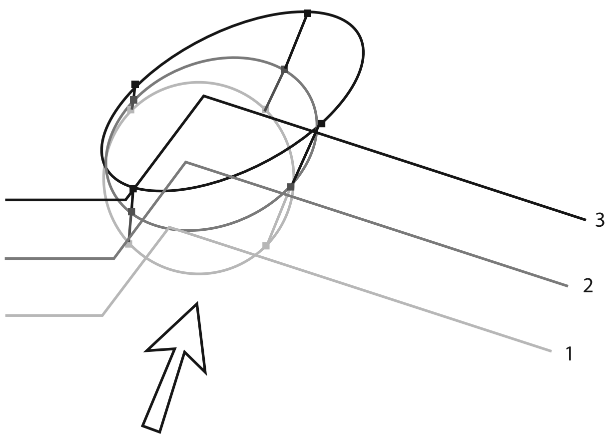

Figure 11. Two-dimensional schematic drawing, illustrating the progressive evolution of the strain ellipse in front of the indenter edge during NNE directed shortening. Particles located east of the indenter edge are displaced to the NNE at a rate comparable to that of the indenter. In contrast, particles located west of the indenter move toward the north at a smaller displacement rate.

Sornette et al., 1993] showed the formation of these conjugate structures. The latter interpretation is also consistent with the results of recent experiments of shortening between parallel plates, hence without an indenter [*Willingshofer et al.*, 2005], which did not show the formation of two major conjugate transpressive faults as described above.

6.5. E-W Extension in Front of the Indenter Corner

[61] E-W extension in front of the indenter corner, i.e., at a site analogous to the Brenner extensional fault in the Eastern Alps (Figures 1a and 1b), was observed in all indentation models with an oblique component of convergence, although it was not very pronounced when the indenter moved to the NNW (Figures 6a and 6b). Particle flow fields show that the area of orogen-parallel extension coincides with a transitional zone, separating particles that flow at higher velocity toward the NNE from particles that flow at a lower velocity in the same direction (Figures 5f and 7c), or at a smaller velocity toward the north (Figures 5c and 6f). As illustrated in Figure 11, E-W extension affected this transitional area in order to maintain compatibility between domains that were shortened in different directions and at different rates. This explains why the only area characterized by significant E-W extension in the model coincides with a major geometrical discontinuity, like the edge of the indenter.

[62] The amount of extension depends on how the indenter convergence is partitioned in front of the NNW striking and ESE striking margins. Experiments performed with NNE directed convergence show that the model particles in front of the long side of the indenter are displaced in a direction subparallel to that imposed by the indenter convergence (Figures 5c and 6f). In contrast, material particles in front of the short side of the indenter are either displaced in a direction that deviates from the movement direction of the indenter, or they remain largely unaffected by indentation (Figures 5c and 6f). As a consequence, a component of lateral (orogen-parallel) extension forms between particles that were originally located west and east of the indenter edge. If the convergence direction is toward the NNE, the long side of the indenter is nearly perpendicular to the convergence direction, hence severely limiting partitioning of deformation into a strike-slip component along this side. In contrast, for the same direction of convergence, the resolved shear stress on the short side of the indenter is large, favoring strike-slip deformation.

6.6. Driving Force of E-W Extension

[63] The driving force of E-W extension has been interpreted as a response to earlier crustal thickening [*Behrmann*, 1988; *Ratschbacher et al.*, 1991b; *Frisch et al.*, 1998, 2000], i.e., as a gravitationally driven process, or as the result of externally driven plate dynamics related to eastward escape of the Eastern Alps [*Selverstone*, 1988, 2005; *Robl and Stüwe*, 2005a], and to extension of the Pannonian basin due to subduction rollback below the Carpathian chain [e.g., *Royden*, 1988; *Sperner et al.*, 2002], or finally, as a combined process, driven by plate tectonic and by gravitational forces [*Ratschbacher et al.*, 1991b]. A recent numerical model [*Robl and Stüwe*, 2005a], suggested that 90% of the eastward displacement was due to tectonic forces and only 10% to gravitational spreading. In addition, *Robl and Stüwe* [2005b] argued that roll back of the subduction zone beneath the Carpathians was insufficient to cause extension in the Eastern Alps.

[64] The absence of an active extensional displacement along the eastern boundary of our models does not allow us to test the effect of subduction rollback in the Carpathians on the deformation pattern of the Eastern Alps. However, the present experiments show that E-W extension in front of the indenter edge can be purely kinematically driven and entirely related to indentation. As discussed above, NNE directed convergence caused extension in front of the indenter edge by displacing all particles located east of the indenter edge to the NE, but hardly affecting material particles west of the indenter edge which remained very close to their initial position (Figures 5c, 5f, and 6f). This divergent motion that caused E-W extension, formed in order to maintain compatibility between two adjacent areas that were shortened at different rates and in different directions.

[65] If extension were gravitationally driven, it would not have occurred at the onset of shortening, because no thickness gradient, hence no gravitational gradient, exists at this stage. During shortening, thickening in front of the indenter edge was much faster than on the eastern end of the indenter, and thus an E-W oriented gradient in potential energy developed, becoming more and more important with increasing amounts of shortening. Therefore, if extension had been gravitationally controlled, the rate of extension should have increased during convergence. However, this was not the case, as seen in Figures 5c and 6f, where the particle flow in front of the indenter edge changed from NE

to north directed during ongoing convergence, thus reducing the component of extension and east directed flow.

[66] Gravitationally driven extension takes place when a lateral gradient in potential energy develops and when the crust is too weak to maintain this gradient. Model X (Figures 7a, 7b, and 7c), in which we reduced the strength of the lower crust in order to favor the nucleation of a detachment, hence gravitationally driven extension, did not show a larger amount of lateral displacement than the models constructed without a lower crustal weakness.

7. Conclusions

[67] In the experiments that we carried out to simulate the oblique indentation in the Eastern Alps, the fault pattern is significantly affected by the rheology of the model lithosphere. Built-in weakness zones control the area of initial deformation, which tends to localize along the margins of the weak zone. However, such weakness zones do not coincide with areas of enhanced lateral displacement. In addition, the deformation pattern resulting from such experiments shows little similarity to the Tertiary deformation pattern of the Eastern Alps.

[68] Minor changes in the angle of convergence affect the pattern of deformation and the particle flow. The models that best reproduced the Tertiary deformation pattern of the Eastern Alps were those with N20°E directed motion of the rigid indenter, which induced a NNE directed displacement of the particles in front of the long side of the indenter. As a consequence, the convergence direction of the South Alpine indenter in the Miocene may also have been directed to the NNE. However, other scenarios can be envisaged, in which the convergence direction of the indenter is partitioned into a complex displacement field (Figure 9). For example, if the indenter motion was partitioned more strongly into dextral strike slip along the indenter margin, north directed convergence could be accommodated by NNE directed shortening in front of the indenter (Figure 9b) [*Handy et al.*, 2005]. Under these conditions, the structures of experiments III and V could also be produced by north directed convergence (Figure 9b). In addition, we cannot preclude that the close similarity between fault patterns of the Eastern Alps and experiment V might also be attained applying different boundary conditions than in our models. The present experiments show that orogen-parallel extension and folding with a spatial distribution resembling the Eastern Alps can form merely in response to indentation.

[69] Assuming a strong coupling between indenter and orogenic crust, sinistral rotation of the Eastern Alps as inferred from paleomagnetic results may be explained by models with oblique, NNE directed convergence. In contrast, north directed and NNW directed convergence in the models lead to dextral rotations.

[70] E-W extension in front of the indenter edge in the experiments was not caused by gravitational instabilities, but rather resulted from the kinematic boundary conditions of the models. The oblique convergence of the indenter caused the local divergent flow in front of the indenter edge, which separated an area moving to the NNE from one moving to the north or NW at a much lower rate. These differences in velocity and direction of the displacement pattern were accommodated by E-W to ENE-WSW extensional deformation in front of the indenter edge. This area has the same structural position as the Brenner extensional fault in the Eastern Alps, which also maintains compatibility between two areas characterized by very different tectonic styles. Whereas the Tauern Window was intensely shortened east of the leading edge of the indenter, Tertiary shortening was very modest further west. The fact that both the Brenner and the Simplon extensional faults (Figure 1a) are located at the leading edge of an indenter supports the interpretation of orogen-parallel extension as a local, albeit significant process, required to maintain compatibilities between adjacent areas that were shortened at different rates and in different directions.

[71] Lateral displacement in the experiments of the present study was always modest, attaining a maximum of ~20% in the models with NNE directed convergence. The deformation patterns of theses experiments were similar to the one observed in the Tertiary Eastern Alps, suggesting that large amounts of orogen-parallel extension are not required to obtain the present-day fault pattern. In addition, our reassessment of data from the literature indicates that the amount of lateral escape in the Eastern Alps has generally been overestimated. We suggest that E-W extension in the Eastern Alps did not exceed 20%, and thus extrapolation of our models to the Tertiary tectonics of the Alps may be realistic.

[72] **Acknowledgments.** J. J. Kermarrec, J. P. Caudal, and J. Smit kindly supported the technical part of the project. We acknowledge the journal reviewers B. Fügenschuh, J. Selverstone, G. Viola, the Associate Editor K. Stüwe, and also the informal review of M. Handy. H.-G. Linzer helped to clarify some methodological aspects of previous determinations of E-W extension in the Eastern Alps. This project has been generously financed by the Deutsche Forschungsgemeinschaft (Ro 2177/2-1).

References

Axen, G. J., J. M. Bartley, and J. Selverstone (1995), Structural expression of a rolling hinge in the footwall of the Brenner Line normal fault, Eastern Alps, *Tectonics*, *14*, 1380–1392.

Barnes, J. D., J. Selverstone, and Z. D. Sharp (2004), Interactions between serpentinite devolatilization, metasomatism and strike-slip strain localization during deep-crustal shearing in the Eastern Alps, *J. Metamorph. Geol.*, *22*, 283–300.

Behrmann, J. H. (1988), Crustal-scale extension in a convergent orogen: The Sterzing-Steinach mylonite zone in the Eastern Alps, *Geodin. Acta*, *2*, 63–73.

Bigi, G., A. Castellarin, M. Coli, G. V. Dal Piaz, M. Sartori, P. Scandone, and G. B. Vai (1990), Structural model of Italy, SELCA, Florence, Italy.

Borsi, S., A. Del Moro, F. P. Sassi, A. Zanferrari, and G. Zirpoli (1978), New geopetrologic and radiometric data on the alpine history of the austridic continental margin south of the Tauern Window (Eastern Alps), *Cons. Naz. Ric.*, *32*, 3–17.

Brun, J.-P. (1999), Narrow rifts versus wide rifts: Inferences for the mechanics of rifting from laboratory experiments, *Philos. Trans. R. Soc. London, Ser. A*, *357*, 695–712.

Brun, J.-P. (2002), Deformation of the continental lithosphere: Insights from brittle-ductile models, in *Deformation Mechanisms, Rheology and Tectonics*, edited by S. De Meer et al., *Geol. Soc. Spec. Publ.*, *200*, 355–370.

Brun, J.-P., and O. Merle (1985), Strain patterns in models of spreading-gliding nappes, *Tectonics*, *4*, 705–719.

Castellarin, A., A. M. Fesce, V. Picotti, G. A. Pini, G. Prosser, R. Sartori, L. Selli, L. Cantelli, and R. Ricci (1987), Structural and kinematic analysis of the Giudicarie deformation belt. Implications for compressional tectonics of southern Alps, *Mineral. Petrogr. Acta*, *30*, 287–310.

Castellarin, A., G. B. Vai, and L. Cantelli (2006), The Alpine evolution of the southern Alps around the Giudicarie faults: A late Cretaceous to early Eocene transfer zone, *Tectonophysics*, *414*, 203–223.

Cobbold, P. R., and P. Davy (1988), Indentation tectonics in nature and experiment. 2. Central Asia, *Bull. Geol. Inst. Univ. Uppsala*, *14*, 143–162.

Cornelius, H. P. (1940), Zur Auffassung der Ostalpen im Sinne der Deckenlehre, *Z. Dtsch. Geol. Ges.*, *92*, 271–312.

Davy, P. H., and P. R. Cobbold (1988), Indentation tectonics in nature and experiments 1. Experiments scaled for gravity, *Bull. Geol. Inst. Uppsala*, *14*, 129–141.

Davy, P., and P. R. Cobbold (1991), Experiments on shortening of a 4–layer continental lithosphere, *Tectonophysics*, *188*, 1–25.

Davy, P., A. Sornette, and D. Sornette (1990), Some consequences of a proposed fractal nature of continental faulting, *Nature*, *348*, 56–58.

Davy, P., A. Hansen, E. Bonnet, and S.-Z. Zhang (1995), Localization and fault growth in layered brittle-ductile systems: Implications for deformations of the continental lithosphere, *J. Geophys. Res.*, *100*, 6281–6294.

Decker, K., H. Peresson, and P. Faupl (1994), Die Miozäne Tektonik der östlichen Kalkalpen: Kinematik, Paläospannungen und Deformationsaufteilung währen der ''lateralen Extrusion'' der Zentralalpen, *Jahrb. Geol. B.-A.*, *1137*, 5–18.

Dewey, J. F. (1988), Extensional collapse of orogens, *Tectonics*, *7*, 1123–1139.

Doglioni, C., and A. Bosellini (1987), Eoalpine and mesoalpine tectonics in the southern Alps, *Geol. Rundsch.*, *76*, 735–754.

Ebbing, J., C. Braitenberg, and H.-J. Götze (2001), Forward and inverse modelling of gravity revealing insight into crustal structures of the Eastern Alps, *Tectonophysics*, *337*, 191–208.

England, P., and G. Houseman (1989), Extension during continental convergence, with application to the Tibetan Plateau, *J. Geophys. Res.*, *94*, 17,561–17,579.

England, P., and P. Molnar (1990), Right-lateral shear and rotation as the explanation for strike-slip faulting in eastern Tibet, *Nature*, *344*, 140–142.

Exner, C. (1962), Sonnblicklamelle und Mölltallinie, *Jahrb. Geol. Bundesanst.*, *105*, 273–286.

Frisch, W., J. Kuhlemann, I. Dunkl, and A. Brügel (1998), Palinspastic reconstruction and topographic evolution of the Eastern Alps during late Tertiary tectonic extrusion, *Tectonophysics*, *297*, 1–15.

Frisch, W., I. Dunkl, and J. Kuhlemann (2000), Post-collisional orogen-parallel large-scale extension in the Eastern Alps, *Tectonophysics*, *327*, 239–265.

Fügenschuh, B., D. Seward, and N. S. Mantckelow (1997), Exhumation in a convergent orogen: The western Tauern window, *Terra Nova*, *9*, 213–217.

Genser, J., and F. Neubauer (1989), Low angle normal faults at the eastern margin of the Tauern window (Eastern Alps), *Mitt. Oest. Geol. Ges.*, *81*, 233–243.

Grenerczy, G., G. Sella, S. Stein, and A. Kenyeres (2005), Tectonic implications of the GPS velocity field in the northern Adriatic region, *Geophys. Res. Lett.*, *32*, L16311, doi:10.1029/2005GL022947.

Handy, M. R., J. Babist, R. Wagner, C. L. Rosenberg, and M. Konrad (2005), Decoupling and its relation to strain partitioning in continental lithosphere—Insight from the Periadriatic Fault System (European Alps), in *Deformation Mechanisms, Rheology and Tectonics: From Minerals to the Lithosphere*, edited by D. Gapais et al., *Geol. Soc. Spec. Publ.*, *243*, 249–276.

Houseman, G., and P. England (1993), Crustal thickening versus lateral expulsion in the Indian-Asian continental collision, *J. Geophys. Res.*, *98*, 12,233–12,249.

Huismans, R. S., Y. Y. Podlachikov, and S. Cloetingh (2001), Dynamic modeling of the transition from passive to active rifting, application to the Pannonian basin, *Tectonics*, *20*, 1021–1039.

Jacobs, J., and R. J. Thomas (2004), Himalayan-type indenter-escape tectonics model for the southern part of the late Neoproterozoic–early Paleozoic East African–Antarctic orogen, *Geology*, *32*, 721–724.

Kleinschrodt, R. (1987), Quarzkorngefügeanalyse im Altkristallin südlich des westlichen Tauernfensters (Südtirol/Italien), *Erlanger Geol. Abh.*, *114*, 1–82.

Kuhlemann, J., W. Frisch, I. Dunkl, and B. Székely (2001), Quantifying tectonic versus erosive denudation: The Miocene core complexes of the Alps, *Tectonophysics*, *330*, 1–23.

Kurz, W., and F. Neubauer (1996), Deformation partitioning during updoming of the Sonnblick area in the Tauern Window (Eastern Alps, Austria), *J. Struct. Geol.*, *18*, 1327–1343.

Kurz, W., W. Unzog, F. Neubauer, and J. Genser (2001), Evolution of quartz microstructures and textures during polyphase deformation within the Tauern Window (Eastern Alps), *Int. J. Earth Sci.*, *90*, 361–378.

Lammerer, B. (1988), Thrust-regime and transpression-regime tectonics in the Tauern Window (Eastern Alps), *Geol. Rundsch.*, *77*, 143–156.

Lammerer, B., and M. Weger (1998), Footwall uplift in an orogenic wedge: The Tauern Window in the Eastern Alps of Europe, *Tectonophysics*, *285*, 213–230.

Laubscher, H. P. (1988), Material balance in Alpine orogeny, *Geol. Soc. Am. Bull.*, *100*, 1313–1328.

Linzer, H.-G., F. Moser, F. Nemes, L. Ratschbacher, and B. Sperner (1997), Build-up and dismembering of a classical fold-thrust belt: From non-cylindrical stacking to lateral extrusion in the eastern northern Calcareous Alps, *Tectonophysics*, *272*, 97–124.

Linzer, H.-G., K. Decker, H. Peresson, R. Dell'Mour, and W. Frisch (2002), Balancing orogenic float of the Eastern Alps, *Tectonophysics*, *354*, 211–237.

Lu, C. Y., and J. Malavieille (1994), Oblique convergence, indentation and rotation tectonics in the Taiwan Mountain Belt: Insights from experimental modeling, *Earth Planet. Sci. Lett.*, *121*, 477–494.

Mancktelow, N. S., and T. L. Pavlis (1994), Fold-fault relationships in low-angle detachment systems, *Tectonics*, *13*, 668–685.

Mancktelow, N. S., D. F. Stöckli, B. Grollimund, W. Müller, B. Fügenschuh, G. Viola, D. Seward, and I. M. Villa (2001), The DAV and Periadriatic fault systems in the Eastern Alps south of the Tauern window, *Int. J. Earth Sci.*, *90*, 593–622.

Martinod, J., D. Hatzfeld, J. P. Brun, P. Davy, and P. Gautier (2000), Continental collision, gravity spreading, and kinematics of Aegean and Anatolia, *Tectonics*, *19*, 290–299.

Márton, E., J. Kuhlemann, W. Frisch, and I. Dunkl (2000), Miocene rotations in the Eastern Alps- paleomagnetic results from intramontane basin sediments, *Tectonophysics*, *323*, 163–182.

Meissner, R., W. D. Mooney, and I. Artemieva (2002), Seismic anisotropy and mantle creep in young orogens, *Geophys. J. Int.*, *149*, 1–14.

Molnar, P., and P. Tapponnier (1977), Relation of the tectonics of eastern China to the India-Eurasia collision: Application of slip-line field theory to large-scale continental tectonics, *Geology*, *5*, 212–216.

Neubauer, F. (1988), Bau und Entwicklungsgeschichte des Rennfeld-Mugel-und des Gleinalm-Kristallins (Ostalpen), *Abh. Geol. Bundesanst*, *42*, 1–137.

Neubauer, F., J. Genser, W. Kurz, and X. Wang (1999), Exhumation of the Tauern Window, Eastern Alps, *Phys. Chem. Earth (A)*, *24*, 675–680.

Ortner, H. (2003), Local and far field stress-analysis of brittle deformation in the western part of the northern Calcareous Alps, Austria, *Geol. Paleontol. Mitt. Innsbruck*, *26*, 109–136.

Peltzer, G. (1988), Centrifuged experiments of continental scale tectonics in Asia, *Bull. Geol. Inst. Univ. Uppsala*, *14*, 115–128.

Peltzer, G., and P. Tapponnier (1988), Formation and evolution of strike-slip faults, rifts and basins during the India-Asia collision: An experimental approach, *J. Geophys. Res.*, *93*, 15,085–15,117.

Peresson, H., and K. Decker (1997), The Tertiary dynamics of the northern Eastern Alps (Austria): Changing palaeostress in a collisional plate boundary, *Tectonophysics*, *272*, 125–157.

Picotti, V., G. Prosser, and A. Castellarin (1995), Structures and kinematics of the Giudicarie-Val Trompia fold and thrust belt (central southern Alps, northern Italy), *Mem. Sci. Geol.*, *47*, 95–109.

Polinski, R. K., and G. H. Eisbacher (1992), Deformation partitioning during polyphase oblique convergence in the Karawanken Mountains, southeastern Alps, *J. Struct. Geol.*, *14*, 1203–1213.

Prosser, G. (1998), Strike-slip movements and thrusting along a transpressive fault zone: The North Giudicarie line (Insubric line, northern Italy), *Tectonics*, *17*, 921–937.

Ratschbacher, L., W. Frisch, F. Neubauer, S. M. Schmid, and J. Neugebauer (1989), Extension in compressional orogenic belts: The Eastern Alps, *Geology*, *17*, 404–407.

Ratschbacher, L., O. Merle, P. Davy, and P. Cobbold (1991a), Lateral extrusion in the Eastern Alps, part 1: Boundary conditions and experiments scaled for gravity, *Tectonics*, *10*, 245–256.

Ratschbacher, L., W. Frisch, and H.-G. Linzer (1991b), Lateral extrusion in the Eastern Alps: part II. Structural analysis, *Tectonics*, *10*, 257–271.

Rey, P., O. Vanderhaeghe, and C. Teyssier (2001), Gravitational collapse of continental lithosphere: Definition, regimes and modes, *Tectonophysics*, *342*, 435–444.

Robl, J., and K. Stüwe (2005a), Continental collision with finite indenter strength: 1. Concept and model formulation, *Tectonics*, *24*, TC4005, doi:10.1029/2004TC001727.

Robl, J., and K. Stüwe (2005b), Continental collision with finite indenter strength: 2. European Alps, *Tectonics*, *24*, TC4014, doi:10.1029/2004TC001741.

Rosenberg, C. L., J.-P. Brun, and D. Gapais (2004), An indentation model of the Eastern Alps and the origin of the Tauern Window, *Geology*, *32*, 997–1000.

Royden, L. H. (1988), Late Cenozoic Tectonics of the Pannonian Basin System, in *The Pannonian Basin, a study in basin evolution*, edited by L. H. Royden and F. Horvath, *AAPG Mem.*, *45*, 27–48.

Schmid, S. M., B. Fügenschuh, E. Kissling, and R. Schuster (2004), Tectonic map and overall architecture of the Alpine orogen, *Eclogae Geol. Helv.*, *97*, 93–117.

Schönborn, G. (1992), Alpine Tectonics and kinematic models of the central southern Alps, *Mem. Sci. Geol. Padova*, *44*, 229–393.

Selverstone, J. (1988), Evidence for east-west crustal extension in the Eastern Alps: Implications for the unroofing history of the Tauern Window, *Tectonics*, *7*, 87–105.

Selverstone, J. (2005), Are the Alps Collapsing?, *Annu. Rev. Earth Planet. Sci.*, *33*, 113–132.

Selverstone, J., G. J. Axen, and J. M. Bartley (1995), Fluid inclusion constraints on the kinematics of footwall uplift beneath the Brenner Line normal fault, Eastern Alps, *Tectonics*, *14*, 264–278.

Seyferth, M., and A. Henk (2004), Syn-convergent exhumation and lateral extrusion in continental collision zones—Insights from three-dimensional numerical models, *Tectonophysics*, *382*, 1–29.

Sokoutis, D., M. Bonini, S. Medvedev, M. Boccaletti, C. J. Talbot, and H. Koyi (2000), Indentation of a continent with a built-in thickness change: Experiment and nature, *Tectonophysics*, *320*, 243–270.

Sornette, A., P. Davy, and D. Sornette (1993), Fault growth in brittle-ductile experiments and the mechanics of continental collisions, *J. Geophys. Res.*, *98*, 12,111–12,139.

Sperner, B., L. Ratschbacher, and M. Nemčok (2002), Interplay between subduction retreat and lateral extrusion: Tectonics of the Western Carpathians, *Tectonics*, *21*(6), 1051, doi:10.1029/2001TC901028.

Tapponnier, P., G. Peltzer, A. Y. LeDain, R. Armijo, and P. Cobbold (1982), Propagating extrusion tectonics in Asia: New insights from experiments with plasticine, *Geology*, *10*, 611–616.

Vanossi, M., C. R. Perotti, and S. Seno (1994), The Maritime Alps arc in the Ligurian and Tyrrhenian systems, *Tectonophysics*, *230*, 75–89.

Viola, G., N. S. Mancktelow, and D. Seward (2001), Late Oligocene-Neogene evolution of Europe-Adria collision: New structural and geochronological evidence from the Giudicarie fault system (Italian Eastern Alps), *Tectonics*, *20*, 999–1020.

Viola, G., F. Odonne, and N. S. Mancktelow (2004), Analogue modelling of reverse fault reactivation in strike-slip and transpressive regimes: Application to the Giudicarie fault system, Italian Eastern Alps, *J. Struct. Geol.*, *26*, 401–418.

Werling, E. (1992), Tonale-, Pejo- und Judicarien-Linie: Kinematik, Mikrostrukturen und Metamorphose von Tektoniten aus räumlich interferierenden aber verschiedenaltrigen Verwerfungszonen, Ph.D. thesis, ETH-Zürich, Zürich.

Willingshofer, E., D. Sokoutis, and J.-P. Burg (2005), Lithospheric-scale analogue modelling of collision zones with a pre-existing weak zone, in *Deformation Mechanisms, Rheology and Tectonics: From Minerals to the Lithosphere*, edited by D. Gapais, J. P. Brun, and P. R. Cobbold, *Geol. Soc. Spec. Publ.*, *243*, 277–294.

J.-P. Brun, F. Cagnard, and D. Gapais, Géosciences Rennes, UMR 6118 CNRS, Université Rennes I, F-35042 Rennes Cedex, France.

C. L. Rosenberg, Fachbereich Geowisssenschaften, Institut für Geologische Wissenschaften, Fachrichtung Geologie, Malteserstr. 74-100, Haus B, D-12249 Berlin, Germany. (cla@zedat.fu-berlin.de)